

# The nuclear actin-containing Arp8 module is a linker DNA sensor driving INO80 chromatin remodeling

Kilian R. Knoll<sup>1,2,9</sup>, Sebastian Eustermann<sup>1,2,9</sup>, Vanessa Niebauer<sup>1,2</sup>, Elisa Oberbeckmann<sup>3</sup>, Gabriele Stoehr<sup>1,2,7</sup>, Kevin Schall<sup>1,2</sup>, Alessandro Tosi<sup>1,2,8</sup>, Marianne Schwarz<sup>1,2,4</sup>, Andrea Buchfellner<sup>5</sup>, Philipp Korber<sup>3</sup> and Karl-Peter Hopfner<sup>1,2,6\*</sup>

**Nuclear actin (N-actin) and actin-related proteins (Arps) are critical components of several chromatin modulating complexes, including the chromatin remodeler INO80, but their function is largely elusive. Here, we report the crystal structure of the 180-kDa Arp8 module of *Saccharomyces cerevisiae* INO80 and establish its role in recognition of extranucleosomal linker DNA. Arp8 engages N-actin in a manner distinct from that of other actin-fold proteins and thereby specifies recruitment of the Arp4-N-actin heterodimer to a segmented scaffold of the helicase-SANT-associated (HSA) domain of Ino80. The helical HSA domain spans over 120 Å and provides an extended binding platform for extranucleosomal entry DNA that is required for nucleosome sliding and genome-wide nucleosome positioning. Together with the recent cryo-electron microscopy structure of INO80<sup>core</sup>-nucleosome complex, our findings suggest an allosteric mechanism by which INO80 senses 40-bp linker DNA to conduct highly processive chromatin remodeling.**

**A** TP-dependent chromatin remodelers shape the spatial and temporal organization of chromatin and generate hallmark features such as regularly spaced nucleosomal arrays flanking nucleosome-depleted regions at promoters<sup>1,2</sup>. Remodelers are generally grouped into four families, INO80, SWI/SNF, ISWI, and CHD, according to sequence similarities within their common Snf2-type ATPase motor domain. They use ATP-dependent DNA translocation to catalyze different types of large-scale nucleosome remodeling reactions—sliding, eviction/assembly, positioning, and editing (histone exchange)<sup>3,4</sup>.

INO80 and SWI/SNF family remodelers are mega-Dalton complexes comprising typically more than 15 different protein subunits<sup>4</sup>. A unifying but poorly understood key feature of these two multi-subunit remodeler families is the presence of N-actin and Arps. *Saccharomyces cerevisiae* possesses altogether ten Arps. Arp4–9 localize to the nucleus as integral, functionally important subunits of INO80 and SWI/SNF remodelers and of the histone acetyl transferase NuA4/TIP60<sup>4–8</sup>. Arp4 and N-actin form an evolutionarily conserved pair in all of these enzymes, except yeast SWI/SNF and RSC, where the Arp4–N-actin pair is replaced by the diverged, but structurally related, Arp7–Arp9 pair. Structural studies of Arp4–N-actin or Arp7–Arp9 revealed binding via their barbed ends to a helical helicase-SANT-associated (HSA) domain N-terminal to the Snf2-type ATPase domain of Swr1 and Sth1, respectively<sup>9–11</sup>. N-actin and nuclear Arps play an essential role in cellular stress response as well as during development<sup>12,13</sup>, and respective genes, encoding, for example, the human Arp4 homolog BAF53, are frequently mutated in cancer<sup>13,14</sup>. However, the precise molecular mechanism explaining the functional importance of N-actin and nuclear Arps remains still largely elusive.

The INO80 complex is particularly intriguing for studying the functional role of actin-fold proteins in the nucleus<sup>6,15</sup>. In addition to N-actin and Arp4, INO80 contains with Arp5 and Arp8 in total four actin-fold proteins and is conserved in this respect from yeast to man<sup>6,16</sup>. INO80 has pivotal functions in gene regulation, replication, and genome maintenance<sup>16,17</sup>, as it slides<sup>15</sup>, edits<sup>18</sup>, and positions<sup>2,19</sup> nucleosomes including the +1 nucleosome at promoter regions<sup>2</sup>. INO80 has a modular architecture<sup>11,16,20,21</sup>. The Ino80 protein subunit, harboring the Snf2-type ATPase motor, is an assembly platform for the other subunits: its N-terminal region interacts in yeast with the species-specific ‘Nhp10 module’ (a subcomplex of INO80 subunits Ies1, Ies3, Ies5, and Nhp10), which regulates the switch-like stimulation of INO80’s nucleosome sliding efficiency by extranucleosomal DNA >40 bp<sup>22</sup>. The middle region of Ino80 contains the HSA domain (Ino80<sup>HSA</sup>), which binds the highly conserved ‘Arp8 module’ composed of N-actin, Arp4, Arp8, Ies4, and Taf14<sup>11,16</sup>. Deletion of Arp8 or the HSA-domain leads to the loss of the whole Arp8 module and results in a remodeling defective INO80 complex<sup>15,16,23</sup>. The C-terminal region of Ino80 forms the equally conserved INO80 core module (INO80<sup>core</sup>), containing the Snf2-type ATPase, Ies2, the Arp5–Ies6 complex, and the Rvb1–Rvb2 heterohexameric AAA-type ATPases. The structure and unified mechanism by which INO80<sup>core</sup> recognizes and remodels the nucleosome core particle (NCP) has been recently revealed at high resolution by cryo-electron microscopy (cryoEM)<sup>24,25</sup>. We uncovered also that the function of INO80<sup>core</sup> as a macromolecular ratchet depends critically on a direct interaction of Arp5 with nucleosomal DNA<sup>24</sup>. It has been proposed that other nuclear Arps could be involved in DNA or nucleosome interactions<sup>23,26,27</sup>.

<sup>1</sup>Department of Biochemistry, Ludwig-Maximilians-Universität München, Munich, Germany. <sup>2</sup>Gene Center, Ludwig-Maximilians-Universität München, Munich, Germany. <sup>3</sup>Chair of Molecular Biology, Biomedical Center, Faculty of Medicine, Ludwig-Maximilians-Universität München, Munich, Germany.

<sup>4</sup>Institute of Biophysics, Ulm University, Ulm, Germany. <sup>5</sup>ChromoTek GmbH, Planegg, Germany. <sup>6</sup>Center for Integrated Protein Science, Ludwig-Maximilians-Universität München, Munich, Germany. <sup>7</sup>Present address: OmicScouts GmbH, Freising, Germany. <sup>8</sup>Present address: Vossius & Partner, Munich, Germany. <sup>9</sup>These authors contributed equally: K.R. Knoll, S. Eustermann. \*e-mail: [hopfner@genzentrum.lmu.de](mailto:hopfner@genzentrum.lmu.de)

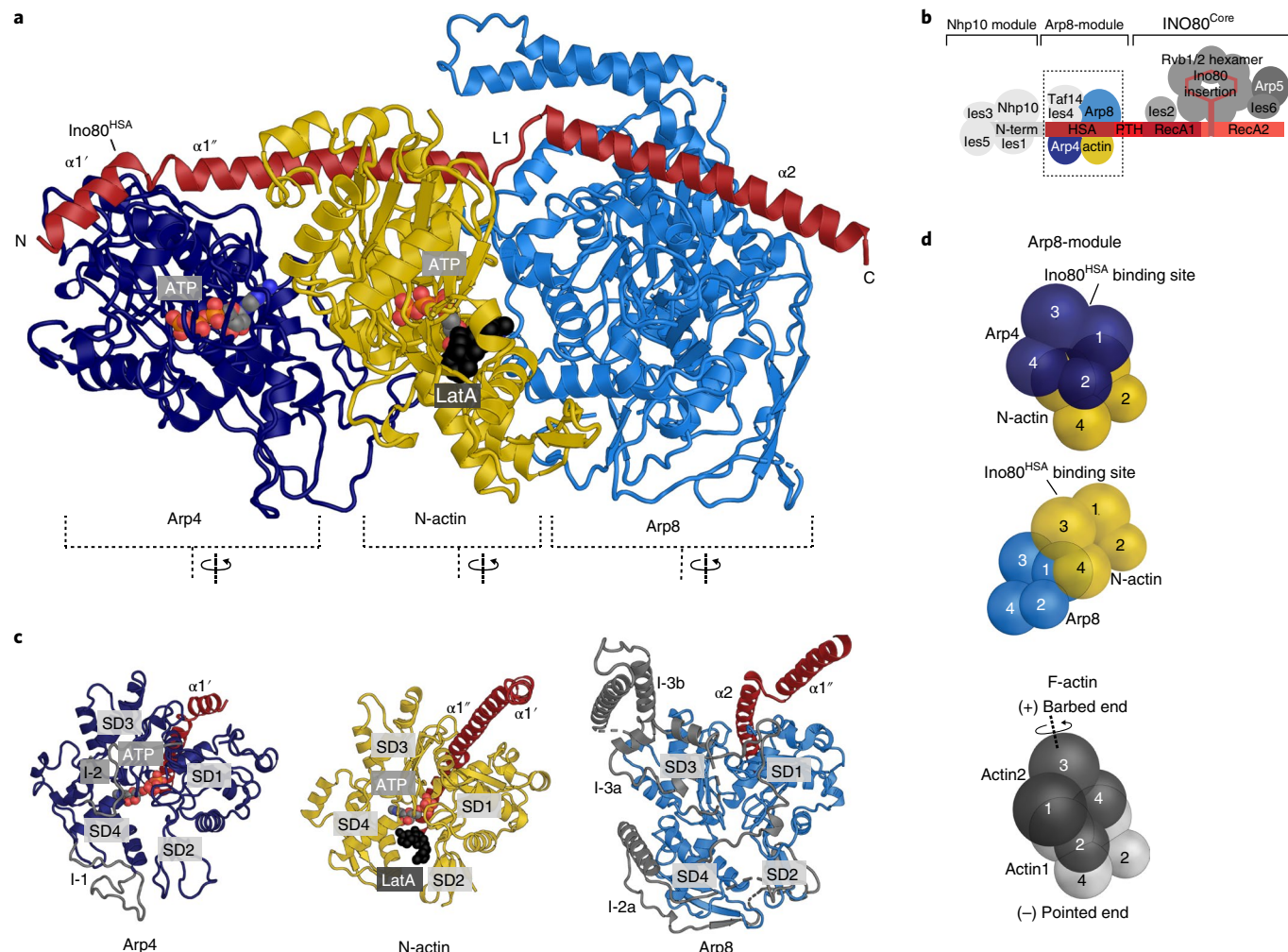


**Fig. 1 | Crystal structure of the 180-kDa Ino80<sup>HSA</sup>-Arp4-N-Actin-Arp8 complex.** **a**, Crystal structure of the INO80 Arp8 module comprising Arp4, N-actin, Arp8, and Ino80<sup>HSA</sup>. Arp4 and N-actin are ATP-bound (colored spheres), whereas Arp8 is nucleotide-free. LatA (black spheres) is bound next to ATP in the N-actin nucleotide binding cleft. **b**, Schematic overview of the *S. cerevisiae* INO80 complex illustrating its modular architecture. N-term, N-terminal region of the Ino80 polypeptide; HSA, HSA domain of Ino80; PTH, post-HSA domain of Ino80. **c**, Front views of the actin-fold proteins Arp4, N-actin, and Arp8. The Ino80<sup>HSA</sup> binds to the barbed end of each of the actin folds. Actin fold insertions of Arp4 and Arp8 are shown in gray. **d**, Arrangement of actin-fold proteins. Schematics of actin folds with the individual subdomains shown as spheres. Interaction of Arp4 with N-actin, and N-actin with Arp8 in the Arp8 module is compared with two laterally interacting actin molecules in F-actin.

Indeed, our cryoEM analysis of a fungal INO80 complex, which included all evolutionarily conserved subunits, located the Arp8 module near extranucleosomal entry DNA, but its analysis was, unlike the NCP-INO80<sup>Core</sup> region of the complex, limited by lower resolution. Until now, high-resolution structural information on the functionally critical architecture of the Arp8 module is missing.

Here, we report the crystal structure of the INO80 Arp8 module and identify it as an allosteric sensor of linker DNA. Strikingly, the Ino80<sup>HSA</sup> adopts a segmented conformation comprising three helices that bind to the barbed ends of Arp4, N-actin, and Arp8. The Arp8 module binds extranucleosomal DNA, and we identified a conserved positively charged patch on the solvent-accessible site of the Ino80<sup>HSA</sup> as responsible for DNA binding. Structure-based mutagenesis showed that binding of extranucleosomal, linker DNA by Ino80<sup>HSA</sup> is critical for INO80 nucleosome sliding, but not for INO80 nucleosome binding and ATP hydrolysis. Thus, linker DNA sensing by the Arp8 module drives remodeling by INO80 via coupling motor activity to nucleosome repositioning.

## Results

**Crystal structure of the 180-kDa Ino80<sup>HSA</sup>-Arp4-N-actin-Arp8 complex.** To gain molecular and functional insights into the evolutionarily conserved Arp8 module of INO80, we determined its crystal structure (Fig. 1). N-actin, Arp4, Arp8 (residues 255–881, excluding the non-conserved N-terminal region<sup>27</sup>), and Ino80<sup>HSA</sup> (residues 461–598) from *S. cerevisiae* were produced in insect cells as a stoichiometric 180-kDa complex (Supplementary Fig. 1a). Initial crystallization attempts failed, most probably due to structural flexibility. In a recent study, N-actin adopted a nucleotide-free state<sup>9</sup> bound to Arp4 and Swr1<sup>HSA</sup>, whereas early biochemical analysis of N-actin in the human BAF complex<sup>28</sup>, as well as our own structural analysis using a camelid nanobody (see below), indicated ATP binding of N-actin. Consequently, we sought to limit the structural heterogeneity of the Arp8 module by using latrunculin A (LatA), a small molecule, sea sponge toxin that inhibits nucleotide exchange of monomeric actin<sup>29</sup>. Addition of LatA yielded crystals of the complex diffracting to 4 Å, and the structure was determined by molecular replacement (see Table 1 for refinement and model statistics).

**Table 1 | Data collection and refinement statistics**

	NactNB-Arp4-N-actin(ATP) (PDB 5NBM)	NactNB-Arp4-N-actin(apo) (PDB 5NBL)	Ino80 <sup>HSA</sup> -Arp4-N-Actin-Arp8 (PDB 5NBN)
<b>Data collection</b>			
Space group	P 6 <sub>5</sub>	P 6 <sub>5</sub>	C 222 <sub>1</sub>
Cell dimensions			
<i>a, b, c</i> (Å)	190.58, 190.58, 220.62	191.22, 191.22, 221.97	172.29, 263.91, 241.40
$\alpha, \beta, \gamma$ (°)	90.00, 90.00, 120.00	90.00, 90.00, 120.00	90.00, 90.00, 90.00
Resolution (Å)	47.73–3.40 (3.50–3.40) <sup>a</sup>	49.43–2.80 (2.90–2.80)	49.40–4.00 (4.10–4.00)
$R_{\text{merge}}$	0.160 (1.081)	0.146 (1.107)	0.236 (1.336)
$I/\sigma(I)$	12.61 (2.19)	12.08 (2.09)	8.71 (1.87)
$CC_{1/2}$	0.996 (0.719)	0.995 (0.617)	0.996 (0.605)
Completeness (%)	100 (100)	100 (100)	100 (100)
Redundancy	6.5 (6.8)	5.9 (5.4)	9.6 (10.0)
<b>Refinement</b>			
Resolution (Å)	47.73–3.40 (3.50–3.40)	49.43–2.80 (2.90–2.80)	49.40–4.00 (4.10–4.00)
No. reflections	62,264 (6,206)	112,476 (11,263)	46,675 (4,625)
$R_{\text{work}}/R_{\text{free}}$	0.152 (0.231)/0.193 (0.281)	0.171 (0.276)/0.204 (0.316)	0.193 (0.254)/0.242 (0.288)
No. atoms			
Protein	13,949	14,000	23,029
Ligand/ion	128 <sup>b</sup>	64 <sup>c</sup>	186 <sup>d</sup>
Water	-	119	-
B factors			
Protein	92.30	58.50	121.87
Ligand/ion	85.97	38.80	101.03
Water	-	48.77	-
R.m.s. deviations			
Bond lengths (Å)	0.004	0.004	0.002
Bond angles (°)	0.66	0.70	0.68

Diffraction data from one NactNB-Arp4-N-actin(ATP), one NactNB-Arp4-N-actin(apo) and one Ino80<sup>HSA</sup>-Arp4-N-Actin-Arp8 crystal were used to solve the structures. <sup>a</sup>Values in parentheses are for highest-resolution shell. <sup>b</sup>Bound ligands are four ATP and four calcium ions. <sup>c</sup>Bound ligands are two ATP and two calcium ions. <sup>d</sup>Bound ligands are two LatA, four ATP, and four calcium ions.

Figure 1 shows the elongated architecture of the Arp8 module. Ino80<sup>HSA</sup> forms a markedly segmented  $\alpha$ -helix with helical elements  $\alpha 1'$ ,  $\alpha 1''$ , and  $\alpha 2$ , spanning a distance of in total 120 Å (Fig. 1a). All three actin-fold proteins bind via their barbed ends to the different HSA helical elements in a similar and serial fashion, while pointed ends remain accessible (Fig. 1c). From Ino80<sup>HSA</sup>'s N to C terminus, the order of binding is Arp4 (to  $\alpha 1'$ ), N-actin (to  $\alpha 1''$ ), and Arp8 (to  $\alpha 2$ ). The segmentation of the HSA helix enables N-actin to form multiple contacts to both Arp4 and Arp8. Arp4 engages N-actin in a ‘front-to-back’ orientation in contrast to the classical fibrous (F) actin ‘front to front’ interaction<sup>30</sup> (Fig. 1d). However, the staggered packing of their subdomains (SDs) as well as local contacts between Arp4 and N-actin resemble lateral interactions of two F-actin subunits in a filament. In contrast, Arp8 packs against the lateral face of N-actin opposite Arp4 by using a fundamentally different ‘side-to-front’ type of interaction, unlike any other seen so far between actin-fold proteins. Interestingly, we observed unambiguous density for ATP in the nucleotide binding pocket of Arp4 and N-actin, whereas Arp8 remains nucleotide-free (Supplementary Fig. 1b,c). Constitutive ATP binding by Arp4 is consistent with our previous observations suggesting that Arp4 is catalytically inactive<sup>26</sup>. However, N-actin may still retain its activity as part of chromatin remodelers<sup>28</sup> and was captured here in its ATP state by LatA. Of note, ATP must have been copurified with the complex from the cellular environment, as we did not add any nucleotides and LatA was added after purification.

**N-actin and Arp4: a conserved heterodimer in distinct chromatin complexes.** Arp4–N-actin within the Arp8 module has an overall configuration similar to Arp4–N-actin bound to Swr1<sup>HSA</sup> and Arp7–Arp9 bound to Snf2<sup>HSA</sup><sup>9,10</sup>, suggesting that the Arp4–N-actin heterodimer is a structurally conserved module within the INO80 and SWI/SNF families.

To probe the Arp4–N-actin heterodimer in its native environment, we capitalized on a nanobody (denoted NactNB) that we generated from an alpaca immunized with the endogenous *S. cerevisiae* INO80 complex. Nanobodies emerged as a valuable technology to reveal physiologically important states of cellular key components<sup>31,32</sup>. NactNB is highly selective for the endogenous Arp4–N-actin heterodimer. Affinity enrichment mass spectrometry of yeast whole-cell lysate using NactNB showed all 35 subunits of chromatin-associated yeast complexes containing the Arp4–N-actin heterodimer (INO80, SWR1, and NuA4) (Fig. 2a,b), suggesting that NactNB recognizes a solvent-exposed and conserved feature in all of these complexes. To reveal this binding epitope, we determined crystal structures of the Arp4–N-actin–NactNB ternary complex (Fig. 2c, Supplementary Fig. 2a, and Table 1). NactNB binds into a crevice jointly formed by the pointed ends of the two actin-folds opposite the Ino80<sup>HSA</sup> binding site (Supplementary Fig. 2b). Satisfyingly, NactNB recognizes the same staggered configuration of N-actin and Arp4, as present in the structure of the Arp8 module (Arp4–N-actin heterodimers align with a backbone r.m.s.d. of 0.68 Å; number of aligned residues

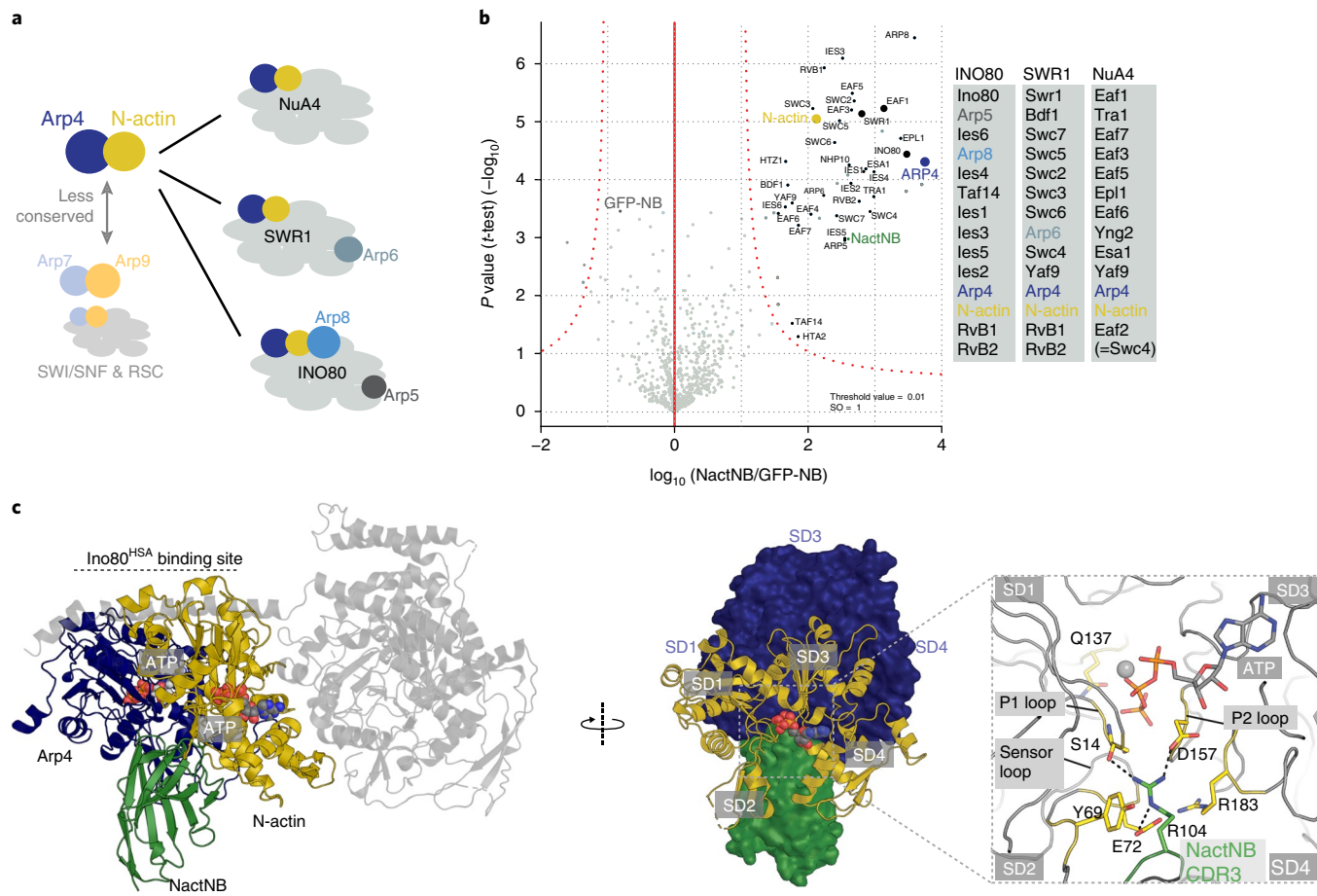


**Fig. 2 | The Arp4-N-actin heterodimer is a conserved structural module of chromatin complexes.** **a**, Arp4 and N-actin are conserved core components of all INO80 and SWI/SNF chromatin remodeler families, except for the *S. cerevisiae* SWI/SNF and RSC remodelers, which instead contain the sequence-divergent Arp7 and Arp9 proteins. INO80 and SWR1 contain the additional Arp5, Arp6, and Arp8 subunits. **b**, NactNB captures endogenous Arp4-N-actin heterodimer. Yeast whole-cell extract was subjected to affinity enrichment mass spectrometry experiments using NactNB and a GFP-binding nanobody as a control. Assays were performed in triplicate, and a two-sided and two-sampled *t*-test shows (in a volcano plot representation) significant enrichment of all 34 subunits of INO80, SWR1, and NuA4 complexes (see Methods for details). **c**, Structure of the Arp4-N-actin-NactNB complex in two orientations shown as cartoon and surface representations (left panel: the Arp8 module structure aligned on the Arp4-N-actin dimer is shown in light gray). N-actin and Arp4 are ATP-bound (colored spheres). Boxed ‘zoom’ image shows that Arg104 of NactNB binds the nucleotide binding cleft of N-actin.

( $N_{\text{align}}$ ) 753 using Secondary Structure Matching<sup>33</sup> in COOT<sup>34</sup>) and in complex with Swr1<sup>HSA</sup> (Arp4-N-actin heterodimers align with an r.m.s.d. of 0.96 Å and  $N_{\text{align}}$  724). Moreover, residual density in the nucleotide binding pocket in absence of added nucleotide as well as cocrystallization with ATP showed that NactNB recognizes the ATP state of N-actin (Supplementary Fig. 2c–e). NactNB detects the relative orientation of the two N-actin lobes and inserts Arg104 in between SD2 and SD4, where it makes hydrogen bonds to the ATP-bound conformation of Ser14 and Asp157 of the phosphate binding loop P1 and P2, respectively, as well as Glu72 of the ATP sensor loop (Fig. 2c).

Taken together, our data provide direct evidence for a conserved configuration of the Arp4-N-actin heterodimer in the complete endogenous INO80, SWR1, and NuA4 complexes and suggest that N-actin can adopt an ATP-bound state in its native environment, as previously also suggested for the human BAF complex<sup>28</sup>. The conserved nature of the Arp4-N-actin heterodimer may point towards a common, yet so far unknown, functional role of this module in distinct chromatin complexes.

**Arp8 recruits Arp4-N-actin to a segmented ‘two-plug’ scaffold of Ino80<sup>HSA</sup>.** Deletion of Arp8 resulted in partially assembled INO80 lacking also Arp4 and N-actin<sup>15,16</sup>. It rendered yeast cells highly

sensitive to metabolic and genotoxic stress<sup>15</sup>. A similar phenotype was observed on partial removal of the Ino80<sup>HSA</sup> and post-HSA domain (Ino80<sup>post-HSA</sup>) (residues 531–598)<sup>23</sup>. The structure of the Arp8 module provides a framework for rationalizing the importance of Arp8 and the Ino80<sup>HSA</sup> for recruitment of the Arp4-N-actin heterodimer to the INO80 complex (Fig. 3a). Arp8 directly engages N-actin through contacts between SD1 and SD2 of Arp8 with SD3 and SD4 of N-actin. In addition, we identify a function for long insertion element I-3a of Arp8. I-3a covers the lateral surface of the Arp8 actin-fold and forms thereby a latch that consolidates the interaction with N-actin. Overall, this bipartite interaction of Arp8 recognizes a 1,392 Å<sup>2</sup> large area of the N-actin lateral face opposite Arp4 and thus specifically helps to recruit and retain the interaction of Arp4-N-actin with Ino80<sup>HSA</sup>.

Previous models proposed that N-actin and Arps are recruited to chromatin remodelers by a long, continuous HSA helix that provides a binding platform for barbed ends of actin-fold proteins<sup>9,10</sup>. While the general helical structure and serial binding of Arp4 and N-actin barbed ends are consistent with this model, Ino80<sup>HSA</sup> adopts a distinct segmented structure (Fig. 3b and Supplementary Fig. 3a,b). The N-terminal helix α1 (residues 472–518), bound to the barbed ends of Arp4 and N-actin, has a pronounced kink at position 483–485 that divides it into segments α1' and α1''. The C-terminal

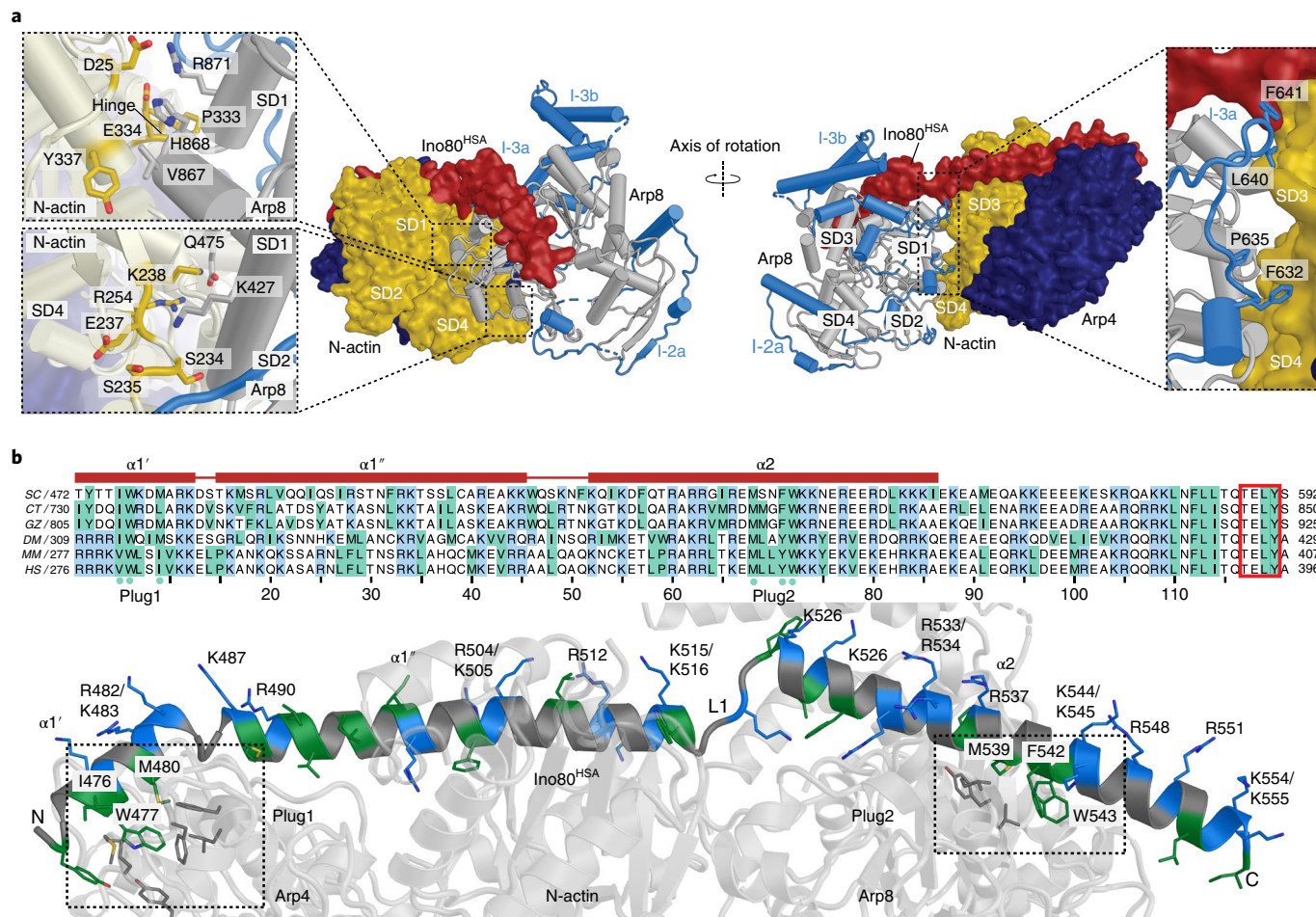


**Fig. 3 | Arp8 recruits Arp4-N-actin to a segmented ‘two-plug’ scaffold of Ino80HSA.** **a**, Cartoon and surface representations of the Arp8 module displaying interaction sites between Arp8 and N-actin. The Arp8 actin core fold is colored in gray and the insertions in blue. Arp8 contacts N-actin SD3 and -4 via its actin core fold, with SD1 and -2 (boxed close-ups in the left panel), and its actin fold insertion 3a (close-up in the right panel). **b**, Sequence alignment of Ino80<sup>HSA</sup> from different species, with positively charged residues (Arg and Lys) colored in blue and hydrophobic residues (Ile, Leu, Trp, Val, Phe, Tyr, and Met) in green. The region visualized in the crystal structure is indicated by red lines above the sequences. The highly conserved TELY motif is highlighted by a red rectangle. Green dots below the sequences emphasize conserved hydrophobic residues in Plug1 and Plug2 that bind Arp4 and Arp8, respectively. Below, cartoon representation of the Arp8 module. The Ino80<sup>HSA</sup> domain is shown, with hydrophobic residues colored in green and positively charged residues colored in blue.

helix  $\alpha 2$  (residues 522–557) forms the third segment, bound to the barbed end of Arp8. We identified two hydrophobic residue clusters (Plug 1 and Plug 2) that define the register and contain each an anchoring tryptophan residue. A structural shift resulting from segmentation of  $\alpha 1$  enables Plug 1 (Ile476, Trp477, and Met480) to insert into a hydrophobic pocket of the barbed end of Arp4 (Fig. 3b and Supplementary Fig. 3c), while well-defined loop L1 in between  $\alpha 1''$  and  $\alpha 2$  shifts  $\alpha 2$ , enabling insertion of Plug 2 (Met539, Phe542, and Trp543) into a hydrophobic pocket of the barbed end of Arp8. The latter interaction appears to be critical not only for recruitment of Arp8 but also of the Arp4–N-actin dimer. The previously reported partial removal of the Ino80<sup>HSA</sup> and Ino80<sup>post-HSA</sup> includes Plug2 of  $\alpha 2$  and leads to loss of the entire Arp8 module *in vivo*<sup>23</sup>, although the Arp4–N-actin binding site of the Ino80<sup>HSA</sup> is still intact. The distance between the two hydrophobic plugs in conjunction with the asymmetry of Ino80<sup>HSA</sup> segmentation matches the unique arrangement of actin-folds within the sandwich-like structure of Arp4, N-actin, and Arp8. In addition, loop L1 and the resulting translational and rotational shift of  $\alpha 2$  enable formation of the extensive contacts between N-actin and Arp8 that would not be

possible for a continuous HSA helix. Thus, our structure shows how Arp8 specifies recruitment of the Arp4–N-actin heterodimer to the segmented, ‘two-plug’ scaffold of the helical Ino80<sup>HSA</sup>.

**Ino80<sup>HSA</sup> of the Arp8 module binds extranucleosomal DNA.** Our recent cryoEM study of the INO80<sup>Core</sup>–nucleosome complex revealed density of the Arp8 module adjacent to the well resolved nucleosomal DNA entry site, where the Ino80 Snf2-motor domain pumps DNA into the nucleosome<sup>24</sup> (Fig. 4a). To test for binding of the Arp8 module to nucleosomal and extranucleosomal DNA, we performed electro mobility shift assays (EMSA) where nucleosomes with (0N80) and without (0N0) 80 bp extranucleosomal DNA on one side compete for binding the Arp8 module (Fig. 4b). In such competition assays, the Arp8 module showed a clear binding preference for the 0N80 over the 0N0 nucleosome, showing that the Arp8 module binds extranucleosomal DNA.

Combination of the INO80<sup>Core</sup>–nucleosome complex cryoEM structure<sup>24</sup> and the Arp8 module crystal structure leads directly to a structural model of how the Arp8 module might be located at extranucleosomal DNA, as discussed further below. In this

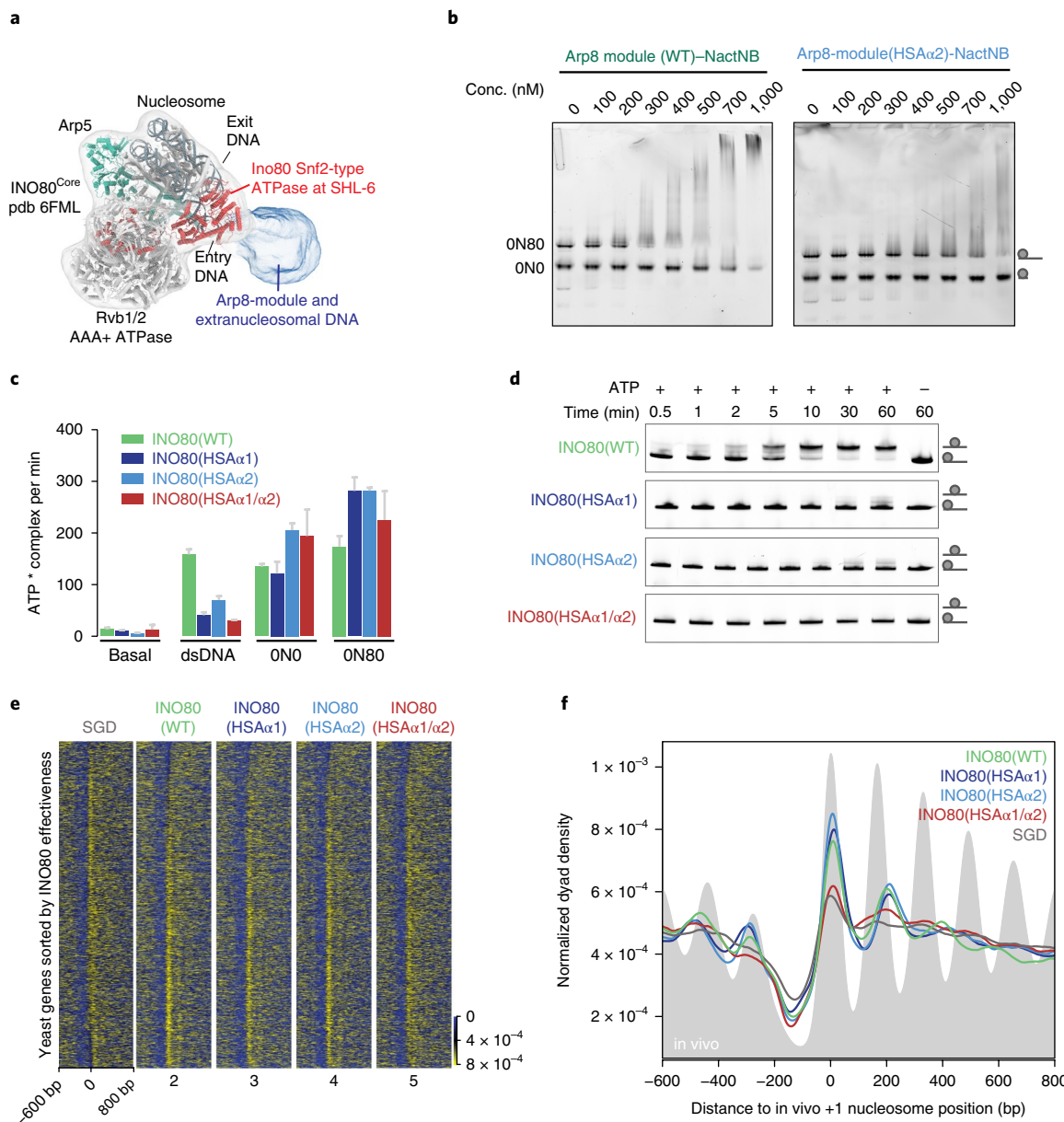


**Fig. 4 | Extranucleosomal DNA binding by the Arp8 module is critical for INO80 nucleosome sliding and genome-wide nucleosome positioning.**

**a**, CryoEM density of the INO80-nucleosome complex<sup>24</sup>, with a structural model for Ino80<sup>Motor</sup>, les2, Arp5, les6, and the Rvb1-Rvb2 heterohexamer bound to an NCP. Density next to the nucleosomal DNA entry site could be assigned to the Arp8 module (colored in blue). **b**, Competition EMSAs with two nucleosome species (20 nM each; one with (ON80) and one without (ONO) an 80-bp extranucleosomal DNA overhang), showing a clear binding preference of the Arp8 module for ON80 nucleosomes. Mutation of solvent-exposed basic residues on helix  $\alpha$ 2 of Ino80<sup>HSA</sup> (HSA $\alpha$ 2) decreases ON80 binding by the Arp8 module. Assays were performed in triplicate. Conc., molar concentration in nM; WT, wild type. **c**, INO80 (27 nM) ATPase activity, basal or stimulated with 223-bp dsDNA (100 nM), ONO (100 nM), and ON80 (50 nM) nucleosomes. Error bars represent the mean  $\pm$  s.d. from three independent experiments. **d**, Time course of ATP-dependent INO80 nucleosome (ON80) sliding on a single mononucleosome substrate (with 18 nM IN80 and 90 nM ON80). Reaction educt (end-positioned nucleosome) and product (center-positioned nucleosome) were resolved by NativePAGE. Assays were performed in triplicate. **e**, Genome-wide nucleosome positioning by INO80 (18 nM). Heat map displaying color-coded nucleosome dyad density of YCp50 plasmid library yeast genes aligned on the in vivo-defined +1 nucleosome dyad (0 bp) position, after sequence-intrinsic nucleosome positioning by salt gradient dialysis (SGD), or after additional incubation with indicated wild-type or mutant INO80 complexes. Rows are sorted according to INO80 effectiveness. **f**, Composite plots of heat maps shown in e. Grey background displays in vivo nucleosome positioning. Genome-wide nucleosome positioning assays were performed in duplicate. Uncropped gel images are shown in Supplementary Data Set 1.

model, Ino80<sup>HSA</sup> mediates direct binding of extranucleosomal DNA along the barbed ends of Arp8, N-actin, and Arp4. In isolation, neither actin and Arp4 nor human Arp8 bind double-stranded DNA (dsDNA) with considerable affinity<sup>26</sup>, while the Ino80<sup>HSA</sup> was proposed from sequence analysis to be part of a dsDNA binding

domain of Ino80<sup>35</sup>. Having the crystal structure for Ino80<sup>HSA</sup>, we noticed a set of highly conserved, solvent-accessible lysine and arginine residues that may account for binding of extranucleosomal DNA (Fig. 3b and Supplementary Fig. 4a). To test this hypothesis, we mutated several of these lysine and arginine residues

in the Ino80<sup>HSA</sup>  $\alpha$ 2 helix to glutamines (HSA $\alpha$ 2). We observed lower expression yields of the mutated minimal Arp8 module, indicating perhaps destabilizing effects of the mutations by lowering the helix propensity of Ino80<sup>HSA</sup>. However, using complex-stabilizing NactNB for purification provided sufficient quantities of stable material for DNA binding studies (Supplementary Fig. 4b). Fluorescence anisotropy analysis on binding of generic 40 bp dsDNA and competition EMSAs with 0N0 and 0N80 nucleosomes showed that binding of NactNB at the pointed end of N-actin only slightly reduced dsDNA binding (around twofold; Supplementary Fig. 4c,d). So, we used NactNB to rule out that any loss of DNA binding is induced by weakening of the complex. Importantly, the  $\alpha$ 2 mutations substantially reduced binding of the Arp8 module both to dsDNA (Supplementary Fig. 4c) and nucleosomes (Fig. 4b and Supplementary Fig. 4d). Thus, we conclude that the positively charged HSA domain of Ino80 provides a binding site for extra-nucleosomal DNA.

**Arp8 module is important for nucleosome sliding and genome-wide nucleosome positioning.** To assess the mechanistic impact of DNA binding by the Arp8 module on nucleosome remodeling by INO80 (Fig. 4), we mutated Ino80<sup>HSA</sup> in the context of the entire INO80 complex (Supplementary Fig. 4e). Parallel to this study, we established an insect cell co-expression approach for expression and purification of the entire *S. cerevisiae* 15-subunit INO80 complex. Such recombinant INO80 retains the activity of the endogenous complex, but is fully amendable to site-directed mutagenesis (to be published elsewhere by: Krietenstein Nils, Oberbeckmann Elisa, Niebauer Vanessa, Schall Kevin, Schwarz Marianne, Moldt Manuela, Tobias Straub, Korber Philipp, Hopfner Karl-Peter, and Eustermann Sebastian). Using this system, we were able to purify stable INO80 complexes with wild-type-like stoichiometry of all subunits, and also if full-length Ino80 with mutated HSA was co-expressed together with all other 14 subunits of INO80 (Supplementary Fig. 4f). EMSAs with 0N80 nucleosomes showed homogenous complex formation at similar concentrations for wild-type as well as for mutant INO80 (Supplementary Fig. 4g). This was in contrast to the decreased binding affinity of Ino80–HSA $\alpha$ 2 in context of the isolated Arp8 module and suggests that binding of the entire complex to nucleosomes is mostly dominated by subunits other than the minimal Arp8 module; for example, subunits of the INO80 core that interact directly with the nucleosome, or other DNA binding subunits such as the Nhp10 module. Of note, Arp8 in the recombinant 15-subunit INO80 complex contains the full N-terminal tail in contrast to the construct used for crystallization. Although the N-terminal region of Arp8 is not well conserved among species, it might additionally contribute to nucleosome interactions, DNA binding, or complex stability.

However, despite retaining high-affinity nucleosome interactions, mutations of the Ino80<sup>HSA</sup> domain markedly affected dsDNA-stimulated ATPase and ATP-dependent nucleosome sliding activity of INO80. ATP hydrolysis by wild-type INO80 is robustly stimulated on addition of dsDNA or 0N80 nucleosomes (Fig. 4c). Mutations of the helix  $\alpha$ 1 or  $\alpha$ 2 of Ino80<sup>HSA</sup> impaired ATPase stimulation by dsDNA, while the same mutants showed similar or even moderately faster ATP hydrolysis rates than wild-type complex if stimulated by 0N80 nucleosomes. Despite this similar or increased ATP turnover, HSA mutations substantially decreased INO80's activity to slide 0N80 nucleosomes towards the center of a 225-bp DNA substrate (Fig. 4d). Mutations of either helix  $\alpha$ 1 or  $\alpha$ 2 reduced nucleosome centering to residual levels, while mutations targeting both helices abrogated this remodeling activity completely.

Given this mechanistic impact on sliding activity in a specialized mononucleosome context, we asked whether Ino80<sup>HSA</sup> is also more generally important to mobilize and position nucleosomes across the whole yeast genome. To this end, we employed a genome-wide

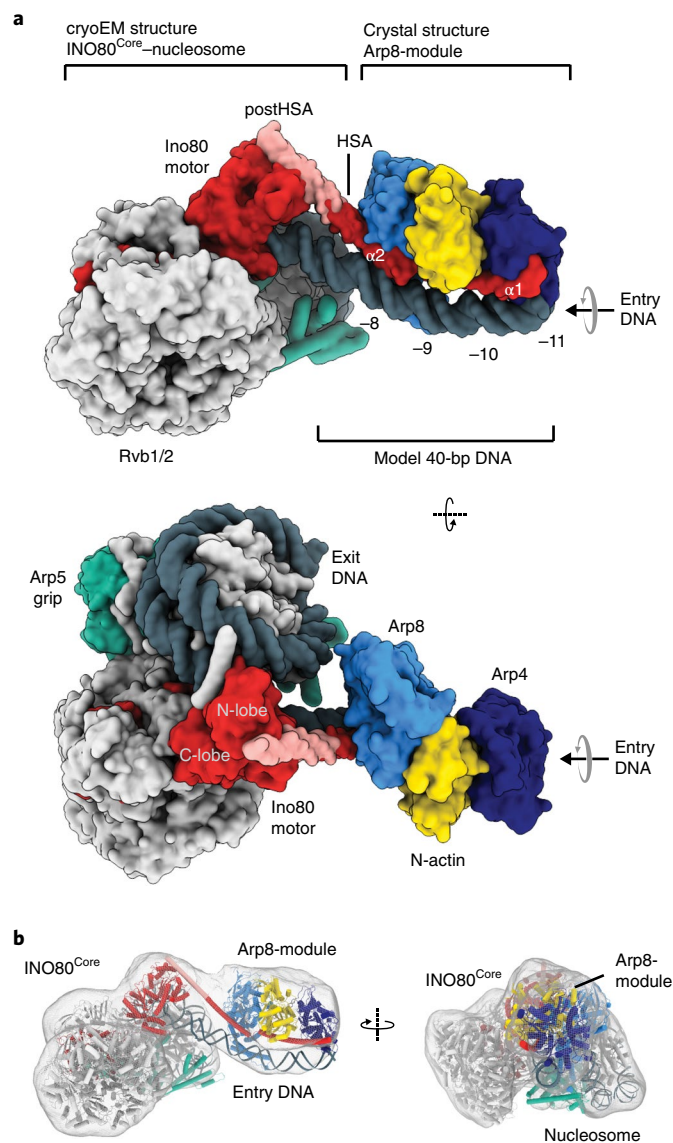


**Fig. 5 | Structural model of the INO80<sup>Core+Arp</sup>-nucleosome complex.**

**a**, Model of the INO80<sup>Core+Arp</sup>-nucleosome complex (shown as surface representation) based on the INO80<sup>Core</sup>-nucleosome cryoEM structure<sup>24</sup> and the Arp8 module crystal structure (this study). **b**, Previously published cryoEM density map of the INO80<sup>Core+Arp</sup>-nucleosome complex<sup>24</sup> with the model of the INO80<sup>Core+Arp</sup>-nucleosome complex fitted into the density.

reconstitution approach, where it was shown previously that purified INO80 on its own is able to properly position +1 nucleosomes on a genomic plasmid library<sup>2</sup>. A similarly direct analysis of INO80's nucleosome positioning activity would be inherently difficult *in vivo*, given the complex interplay between different remodeler families as well as other factors such as the transcription and replication machinery<sup>3,6</sup>. Micrococcal nuclease digestion and next generation DNA sequencing (MNase-seq) was used as read out for nucleosome positions across the genomic plasmid library before and after incubation with INO80 and ATP. In contrast to the strongly decreased sliding activity with a mononucleosomal substrate based on the 'Widom 601' sequence (Fig. 4d), INO80 mutations targeting HSA helix  $\alpha$ 1 or  $\alpha$ 2 individually did not compromise average patterns of genomic +1 nucleosome positioning (Fig. 4e,f). This finding is intriguing as it suggests that nucleosomes on genomic DNA in plasmids may be a less demanding substrate for translocation and positioning than a 'Widom 601' mononucleosome. This could be,

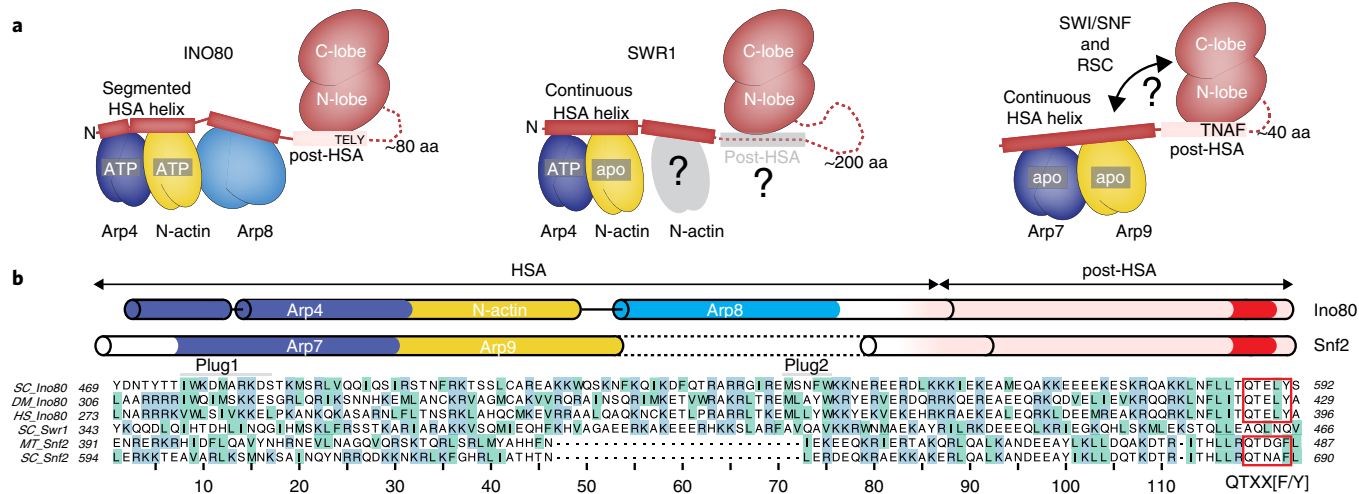


**Fig. 6 | Conserved architecture of N-actin-Arp modules in INO80/SWR1 and SWI/SNF family chromatin remodelers.** **a**, Organization of the N-actin-Arp modules in INO80, SWR1, and RSC remodelers with respect to the Snt2-type ATPase. The schematic representation is based on our Ino80<sup>Core+Arp</sup>-nucleosome model (shown in Fig. 5a), the structure-based sequence alignment shown in **b**, and the crystal structures of Arp4-N-actin-Swr1<sup>HSA</sup> (PDB 519E), Arp7-Arp9-Snf2<sup>HSA</sup> (PDB 4I6M), Arp4-N-actin-Arp8-Ino80<sup>HSA</sup>, and Snt2 in complex with a nucleosome (PDB 5HZR). Conformation of the respective HSA domains (red) is illustrated by a continuous or segmented helix. The post-HSA of Ino80 and Snt2 (pink) interacts directly with N-lobe of the Snt2-type ATPase (red) and is connected via a linker region (dotted line). The nucleotide state of the actin-fold proteins is indicated according to the respective crystal structure. Interestingly, recent biochemical analysis suggested that the Swr1<sup>HSA</sup> is bound by Arp4 and two N-actin molecules<sup>49</sup>. Our structure-based alignment shown in **b** reveals that the Arp8 binding site of Ino80<sup>HSA</sup> corresponds to the second N-actin site in Swr1<sup>HSA</sup>. **b**, Structure-based sequence alignment of the HSA and post-HSA domains of Ino80, Snt2, and Swr1 (basic and hydrophobic residues are highlighted in blue and light green, respectively). Binding sites for Arps and N-actin are conserved between the INO80 and SWI/SNF remodeler families. Our structure-based alignment reveals that the Ino80<sup>post-HSA</sup> (Q)TELY motif is related to the Snt2<sup>post-HSA</sup> QTXX[F/Y] motif.

for example, due to the presence of multiple nucleosomes, extranucleosomal DNA on both sides, the absence of DNA ends, or due to lower intrinsic nucleosome stabilities. The former three possibilities seemed unlikely as remodeling an internal nucleosome within an array of 601 sequences separated by 50 bp extranucleosomal DNA<sup>37</sup> was also strongly impaired by mutations targeting either HSA helix individually (Supplementary Fig. 4h,i). Importantly, however, mutation of both HSA helices  $\alpha 1$  and  $\alpha 2$  at the same time abolished INO80 nucleosome remodeling on all tested substrates including genome-wide nucleosome positioning (Fig. 4d-f and Supplementary Fig. 4i).

Taken together, our biochemical results identify a critical role for binding extranucleosomal DNA by the Arp8 module in coupling the energy derived from ATP hydrolysis to productive nucleosome sliding by INO80. Such chemo-mechanical coupling may be particularly important to mobilize nucleosomes in the context of sequences that strongly bind the histone octamer, such as the 601 sequence. Positioning of +1 nucleosomes guided by promoter sequences is likely to involve also other parts of the INO80 complex, such as the Nhp10 module.

**A structural model of the INO80-nucleosome complex including its Arp8 module.** Combination of the 4.3-Å cryoEM structure of the *C. thermophilum* INO80<sup>Core</sup>-nucleosome complex<sup>24</sup> with the 4-Å *S. cerevisiae* crystal structure of the 180-kDa Arp8 module leads directly to a composite model of the evolutionarily conserved INO80<sup>Core+Arp</sup> complex bound to a nucleosome with a molecular weight of approximately 1 MDa (Fig. 5a). The two structures can be joined in silico by the highly conserved post-HSA and HSA domains of Ino80: helix  $\alpha 2$  of the HSA domain crystal structure needs to be extended by only 35 C-terminal residues to include the post-HSA helix that is present in the cryoEM structure<sup>24</sup>. This structural model is consistent with the mapping of INO80 subunits onto nucleosomal substrates in vivo<sup>38</sup>, in vitro<sup>39</sup>, and with our previous cryoEM

data<sup>24</sup> as it places the Arp8 module into the large unassigned density patch (Figs. 4a and 5b) and at the same time maintains a continuous HSA and post-HSA helical structure. In particular, we observed cryoEM density for an extended post-HSA-HSA helix pointing from the N-terminal lobe of the Snt2-type ATPase domain at SHL-6 towards entry DNA at SHL-8<sup>24</sup>. Moreover, the elongated architecture of the Arp8 module accommodates approximately 40 bp extranucleosomal entry DNA and fits thereby into the low-resolution reconstruction obtained for the entire 11-subunit INO80<sup>Core+Arp</sup>-nucleosome complex<sup>24</sup>. The 120-Å HSA domain is positioned along the dsDNA with conserved arginine and lysine residues contacting the phosphate backbone as probed by our biochemical experiments described above. Helix  $\alpha 2$  contacts the DNA around SHL-8 while the N-terminal helix  $\alpha 1$  reaches SHL-10 to -11. Consequently, Arp8 resides on the extranucleosomal DNA proximal to the Snt2-type ATPase of Ino80, while the Arp4-N-actin heterodimer binds in a distal position. The model is therefore consistent with promoter binding of Arp8 proximal to the +1 nucleosome in vivo<sup>38</sup>, as well as cross-linking of Arp4-N-actin heterodimer to extranucleosomal DNA at position -110 nt (SHL-11) in vitro<sup>39</sup>. However, given the flexibility of the Arp8 module in the cryoEM reconstructions, we do not rule out the presence of other conformations and positions of this module during the functional cycle of INO80 in nucleosome remodeling.

## Discussion

Here, we provide a structure and function for the enigmatic, evolutionarily conserved actin-fold subunits Arp4, N-actin, and Arp8 in the INO80 chromatin remodeler. We show that the three actin-fold proteins in complex with the Ino80<sup>HSA</sup> form an extended structural element that recognizes extranucleosomal, linker DNA, a critical feature of INO80 mechanism and function.

INO80 is a highly processive chromatin remodeler<sup>22,40</sup> and we recently proposed a mechanism by which INO80 core subunits

function as a macromolecular ratchet<sup>24</sup>: minor groove tracking by the Ino80 Snf2-type ATPase motor at SHL-6 pumps DNA in multiple 1–2 bp steps against a grip formed by Arp5–Ies6 at SHL-2/-3 until DNA propagates around the histone octamer and translocates nucleosomes by a large step size. Indeed, 10–20 bp translocation steps are observed<sup>22,41</sup>, and a kinetic model has been proposed describing the dependency of INO80 on extranucleosomal DNA<sup>22</sup>: the activity of the ATPase motor does not result in efficient DNA translocation unless more than 40 bp of entry DNA are available; the pumped DNA might otherwise collapse backwards<sup>22</sup>. Intriguingly, the footprint of the Arp8 module matches this limiting length of 40 bp DNA (Fig. 5a). If less than 40 bp extranucleosomal linker DNA are available, pumping an additional 10–20 bp DNA into the nucleosome would substantially shorten the entry DNA beyond this limit; that is, pull away the DNA and thereby abrogate the contacts between DNA and the distal part of the HSA domain, where the Arp4–N-actin heterodimer binds. Consequently, this scenario recapitulates the impact of HSA mutations that also lead to loss of extranucleosomal DNA binding and reduce nucleosome sliding to residual levels, most probably caused by ‘back-slippage’ of DNA. By combining our structural and biochemical data with previous kinetic insights<sup>22</sup>, we thus propose that the Arp8 module within INO80 functions as sensor of extranucleosomal DNA, mechanistically coupling ATP-dependent DNA pumping to processive nucleosome translocation.

Biochemical and genetic evidence for the SWI/SNF chromatin remodeler family suggests that the yeast Arp7–Arp9 module of RSC has a role similar to that proposed here for the Arp8 module of INO80, as it also couples ATP-dependent DNA translocation of the Snf2-type Sth1 motor domain to nucleosome remodeling such as translocation and ejection<sup>42</sup>. It was proposed that the post-HSA domain of Sth1 acts as a ‘throttle’ controlling ATPase activity<sup>42</sup>. Indeed, our structural study shows that the post-HSA domain interacts with the N-lobe of Ino80<sup>24</sup> in a homologous manner as previously observed for Snf2<sup>43</sup> and Sth1<sup>44</sup>. A structure-based alignment reveals that the highly conserved (Q)TELY motif<sup>b</sup> of the Ino80<sup>post-HSA</sup> domain is related to the QTXX[F/Y] motif of Snf2 (Fig. 6a,b), while the interaction with protrusion-I provides, together with brace helix-I, a key allosteric site for controlling DNA groove tracking by the ATPase motor<sup>42,43</sup>. Despite recent progress<sup>10,42,44,45</sup>, it is still elusive how the Arp7–Arp9 module of RSC functions at a molecular level. It was suggested that the module folds back onto the Sth1 motor domain acting as ‘clutch’ to promote nucleosome remodeling. While INO80 might adopt a closed conformation in absence of a nucleosome<sup>46,47</sup>, our structural and biochemical data suggest an extended conformation of the Arp8 module which enables extranucleosomal DNA binding. The interplay between the HSA and post-HSA domains may thus link sensing of extranucleosomal DNA to allosteric control of the Snf2-like motor domain of Ino80.

Sensing of linker DNA is a hallmark of chromatin remodelers since it provides mechano-chemical means to conduct higher order remodeling reactions such as spacing and phasing of nucleosomes in genic arrays<sup>4,48</sup>. Future studies will use the mechanistic insights discovered here as a framework to dissect such functions and will show whether they may provide unifying principles for regulation of the INO80 and SWI/SNF families of multi-subunit chromatin remodelers.

## Methods

Methods, including statements of data availability and any associated accession codes and references, are available at <https://doi.org/10.1038/s41594-018-0115-8>.

Received: 24 April 2018; Accepted: 17 July 2018;  
Published online: 03 September 2018

## References

- Jiang, C. & Pugh, B. F. Nucleosome positioning and gene regulation: advances through genomics. *Nat. Rev. Genet.* **10**, 161–172 (2009).
- Krietenstein, N. et al. Genomic nucleosome organization reconstituted with pure proteins. *Cell* **167**, 709–721.e12 (2016).
- Hopfner, K. P., Gerhold, C. B., Lakomek, K. & Wollmann, P. Swi2/Snf2 remodelers: hybrid views on hybrid molecular machines. *Curr. Opin. Struct. Biol.* **22**, 225–233 (2012).
- Clapier, C. R., Iwasa, J., Cairns, B. R. & Peterson, C. L. Mechanisms of action and regulation of ATP-dependent chromatin-remodeling complexes. *Nat. Rev. Mol. Cell Biol.* **18**, 407–422 (2017).
- Dion, V., Shimada, K. & Gasser, S. M. Actin-related proteins in the nucleus: life beyond chromatin remodelers. *Curr. Opin. Cell Biol.* **22**, 383–391 (2010).
- Shen, X., Mizuguchi, G., Hamiche, A. & Wu, C. A chromatin remodelling complex involved in transcription and DNA processing. *Nature* **406**, 541–544 (2000).
- Peterson, C. L., Zhao, Y. & Chait, B. T. Subunits of the yeast SWI/SNF complex are members of the actin-related protein (ARP) family. *J. Biol. Chem.* **273**, 23641–23644 (1998).
- Cairns, B. R., Erdjument-Bromage, H., Tempst, P., Winston, F. & Kornberg, R. D. Two actin-related proteins are shared functional components of the chromatin-remodeling complexes RSC and SWI/SNF. *Mol. Cell* **2**, 639–651 (1998).
- Cao, T. et al. Crystal structure of a nuclear actin ternary complex. *Proc. Natl Acad. Sci. USA* **113**, 8985–8990 (2016).
- Schubert, H. L. et al. Structure of an actin-related subcomplex of the SWI/SNF chromatin remodeler. *Proc. Natl Acad. Sci. USA* **110**, 3345–3350 (2013).
- Szerlong, H. et al. The HSA domain binds nuclear actin-related proteins to regulate chromatin-remodeling ATPases. *Nat. Struct. Mol. Biol.* **15**, 469–476 (2008).
- Meagher, R. B., Kandasamy, M. K., Smith, A. P. & McKinney, E. C. Nuclear actin-related proteins at the core of epigenetic control. *Plant Signal. Behav.* **5**, 518–522 (2010).
- Son, E. Y. & Crabtree, G. R. The role of BAF (mSWI/SNF) complexes in mammalian neural development. *Am. J. Med. Genet. C* **166C**, 333–349 (2014).
- Hodges, C., Kirkland, J.G. & Crabtree, G.R. The many roles of BAF (mSWI/SNF) and PBAF complexes in cancer. *Cold Spring Harb. Perspect. Med.* **6**, (2016).
- Shen, X., Ranallo, R., Choi, E. & Wu, C. Involvement of actin-related proteins in ATP-dependent chromatin remodeling. *Mol. Cell* **12**, 147–155 (2003).
- Tosi, A. et al. Structure and subunit topology of the INO80 chromatin remodeler and its nucleosome complex. *Cell* **154**, 1207–1219 (2013).
- Gerhold, C. B. & Gasser, S. M. INO80 and SWR complexes: relating structure to function in chromatin remodeling. *Trends Cell Biol.* **24**, 619–631 (2014).
- Papamichos-Chronakis, M., Watanabe, S., Rando, O. J. & Peterson, C. L. Global regulation of H2A.Z localization by the INO80 chromatin-remodeling enzyme is essential for genome integrity. *Cell* **144**, 200–213 (2011).
- Udugama, M., Sabri, A. & Bartholomew, B. The INO80 ATP-dependent chromatin remodeling complex is a nucleosome spacing factor. *Mol. Cell. Biol.* **31**, 662–673 (2011).
- Chen, L. et al. Subunit organization of the human INO80 chromatin remodeling complex: an evolutionarily conserved core complex catalyzes ATP-dependent nucleosome remodeling. *J. Biol. Chem.* **286**, 11283–11289 (2011).
- Jonsson, Z. O., Jha, S., Wohlschlegel, J. A. & Dutta, A. Rvb1p/Rvb2p recruit Arp5 and assemble a functional Ino80 chromatin remodeling complex. *Mol. Cell* **16**, 465–477 (2004).
- Zhou, C. Y. et al. The yeast INO80 complex operates as a tunable DNA length-sensitive switch to regulate nucleosome sliding. *Mol. Cell* **69**, 677–688.e9 (2018).
- Kapoor, P., Chen, M., Winkler, D. D., Luger, K. & Shen, X. Evidence for monomeric actin function in INO80 chromatin remodeling. *Nat. Struct. Mol. Biol.* **20**, 426–432 (2013).
- Eustermann, S. et al. Structural basis for ATP-dependent chromatin remodelling by the INO80 complex. *Nature* **556**, 386–390 (2018).
- Ayala, R. et al. Structure and regulation of the human INO80–nucleosome complex. *Nature* **556**, 391–395 (2018).
- Gerhold, C. B. et al. Structure of Actin-related protein 8 and its contribution to nucleosome binding. *Nucleic Acids Res.* **40**, 11036–11046 (2012).
- Saravanan, M. et al. Interactions between the nucleosome histone core and Arp8 in the INO80 chromatin remodeling complex. *Proc. Natl Acad. Sci. USA* **109**, 20883–20888 (2012).
- Zhao, K. et al. Rapid and phosphoinositol-dependent binding of the SWI/SNF-like BAF complex to chromatin after T lymphocyte receptor signaling. *Cell* **95**, 625–636 (1998).
- Dominguez, R. & Holmes, K. C. Actin structure and function. *Annu. Rev. Biophys.* **40**, 169–186 (2011).

30. von der Ecken, J. et al. Structure of the F-actin-tropomyosin complex. *Nature* **519**, 114–117 (2015).
31. Huang, W. et al. Structural insights into micro-opioid receptor activation. *Nature* **524**, 315–321 (2015).
32. Rasmussen, S. G. et al. Crystal structure of the beta2 adrenergic receptor-Gs protein complex. *Nature* **477**, 549–555 (2011).
33. Krissinel, E. & Henrick, K. Secondary-structure matching (SSM), a new tool for fast protein structure alignment in three dimensions. *Acta Crystallogr. D Biol. Crystallogr.* **60**, 2256–2268 (2004).
34. Emsley, P., Lohkamp, B., Scott, W. G. & Cowtan, K. Features and development of Coot. *Acta Crystallogr. D Biol. Crystallogr.* **66**, 486–501 (2010).
35. Bakshi, R., Prakash, T., Dash, D. & Brahmachari, V. In silico characterization of the INO80 subfamily of SWI2/SNF2 chromatin remodeling proteins. *Biochem. Biophys. Res. Commun.* **320**, 197–204 (2004).
36. Yen, K., Vinayachandran, V., Batta, K., Koerber, R. T. & Pugh, B. F. Genome-wide nucleosome specificity and directionality of chromatin remodelers. *Cell* **149**, 1461–1473 (2012).
37. Mueller-Planitz, F., Klinker, H., Ludwigsen, J. & Becker, P. B. The ATPase domain of ISWI is an autonomous nucleosome remodeling machine. *Nat. Struct. Mol. Biol.* **20**, 82–89 (2013).
38. Yen, K., Vinayachandran, V. & Pugh, B. F. SWR-C and INO80 chromatin remodelers recognize nucleosome-free regions near +1 nucleosomes. *Cell* **154**, 1246–1256 (2013).
39. Brahma, S., Ngubo, M., Paul, S., Udugama, M. & Bartholomew, B. The Arp8 and Arp4 module acts as a DNA sensor controlling INO80 chromatin remodeling. *Nat. Commun.* <https://doi.org/10.1038/s41467-018-05710-7> (2018).
40. Schwarz, M. et al. Single-molecule nucleosome remodeling by INO80 and effects of histone tails. *FEBS Lett.* **592**, 318–331 (2018).
41. Brahma, S. et al. INO80 exchanges H2A.Z for H2A by translocating on DNA proximal to histone dimers. *Nat. Commun.* **8**, 15616 (2017).
42. Clapier, C. R. et al. Regulation of DNA translocation efficiency within the chromatin remodeler RSC/Sth1 potentiates nucleosome sliding and ejection. *Mol. Cell* **62**, 453–461 (2016).
43. Liu, X., Li, M., Xia, X., Li, X. & Chen, Z. Mechanism of chromatin remodelling revealed by the Snf2-nucleosome structure. *Nature* **544**, 440 (2017).
44. Turegun, B., Baker, R. W., Leschziner, A. E. & Dominguez, R. Actin-related proteins regulate the RSC chromatin remodeler by weakening intramolecular interactions of the Sth1 ATPase. *Commun. Biol.* **1**, 1 (2018).
45. Turegun, B., Kast, D.J. & Dominguez, R. Subunit Rtt102 controls the conformation of the Arp7/9 heterodimer and its interactions with nucleotide and the catalytic subunit of SWI/SNF remodelers. *J. Biol. Chem.* (2013).
46. Aramayo, R. J. et al. Cryo-EM structures of the human INO80 chromatin-remodeling complex. *Nat. Struct. Mol. Biol.* **25**, 37–44 (2018).
47. Watanabe, S. et al. Structural analyses of the chromatin remodelling enzymes INO80-C and SWR-C. *Nat. Commun.* **6**, 7108 (2015).
48. Yamada, K. et al. Structure and mechanism of the chromatin remodelling factor ISW1a. *Nature* **472**, 448–453 (2011).
49. Lin, C.-L. et al. Functional characterization and architecture of recombinant yeast SWR1 histone exchange complex. *Nucleic Acids Res.* **45**, 7249–7260 (2017).

## Acknowledgements

We are grateful to M. Moldt for technical support and J. Michaelis, Gregor Witte, Katja Lames, and Robert Byrne for discussion and technical help. We thank the Max-Planck Crystallization Facility (Martinsried, Germany), the staff of the Swiss Light Source (Villigen, Switzerland), and the European-Molecular-Biology-Laboratory/Deutsches-Elektronen-Synchrotron (Hamburg, Germany) for support and measurement time. We thank S. Krebs and H. Blum at the Laboratory of Functional Genome Analysis (Gene Center, LMU Munich) for high-throughput sequencing. We thank T. Straub (Bioinformatics Core Unit, Biomedical Center, LMU Munich) for advice on bioinformatics. This work is supported by the Deutsche Forschungsgemeinschaft CRC1064 (to K.-P.H. and P.K.) and the European Research Council (ERC Advanced Grant ATMMACHINE), the Gottfried-Wilhelm-Leibniz Prize, and the Center for Integrated Protein Sciences Munich to K.-P.H. K.R.K. is supported by GRK1721. S.E. acknowledges an EMBO long-term fellowship. V.N., K.S., and M.S. acknowledge funding by Quantitative Biosciences Munich.

## Author contributions

K.R.K. and S.E. determined the structures and built atomic models. K.R.K. prepared samples for crystallization and performed biochemical analysis of the Arp8 module. S.E., A.T., M.S., and A.B. identified the Arp4-N-actin binding nanobody and performed its initial characterization. K.R.K. and G.S. performed affinity enrichment mass spectrometry analysis. S.E. and K.P.H. devised with a contribution of M.S. preparation and characterization of recombinant INO80 complex. V.N. prepared mutant complexes and performed their biochemical analysis. V.N. and E.O. performed and analyzed genome-wide remodeling assays under supervision by P.K. K.S. prepared nucleosomes. S.E. and K.-P.H. designed the overall study, analyzed the results, and wrote the paper with contributions from K.R.K., V.N., E.O., and P.K.

## Competing interests

The authors declare no competing interests.

## Additional information

**Supplementary information** is available for this paper at <https://doi.org/10.1038/s41594-018-0115-8>.

**Reprints and permissions information** is available at [www.nature.com/reprints](http://www.nature.com/reprints).

**Correspondence and requests for materials** should be addressed to K.-P.H.

**Publisher's note:** Springer Nature remains neutral with regard to jurisdictional claims in published maps and institutional affiliations.

## Methods

**Nanobody generation.** For generation of the Arp4–N-actin binding nanobody (NactNB), an alpaca was immunized with purified and cross-linked endogenous INO80 complex. INO80 complex for immunization was prepared as earlier described<sup>16</sup>. Alpaca immunization, nanobody library generation, and selection of INO80 binding nanobodies were performed as previously published<sup>30</sup> by ChromoTek GmbH.

**Cloning, protein expression, and purification.** *Nanobody (NactNB).* The DNA sequence coding NactNB carrying a C-terminal Twin-Strep-Tag was cloned into a pHEN6 vector upstream of the pelB leader sequence<sup>51</sup>. *Escherichia coli* Rosetta (DE3) cells (Merck Millipore) were transformed with the pHEN6-NactNB vector. Freshly transformed cells were cultured at 37 °C in lysogeny broth containing 100 µg ml<sup>-1</sup> ampicillin. Protein was expressed for 2 h at 22 °C after induction with 0.3 mM isopropyl β-D-thiogalactopyranoside at an optical density at 600 nm of 0.6. All protein purification steps were performed at 4 °C. Cells were collected by centrifugation and subsequently incubated for 30 min in lysis buffer (50 mM Tris pH 8.0, 300 mM NaCl, 1× protease inhibitor cocktail (Sigma-Aldrich), 1 mg ml<sup>-1</sup> lysozyme (Carl Roth), and 12.5 units ml<sup>-1</sup> benzonase (unit is a measure for the amount of the enzyme and defined by the vendor Sigma-Aldrich)) for periplasmic lysis. The cell debris were separated by centrifugation. NactNB was purified from the soluble extract via the C-terminal Twin-Strep-Tag using Strep-Tactin Sepharose (IBA) in 50 mM Tris pH 8.0 and 300 mM NaCl. NactNB bound to Strep-Tactin Sepharose was stored at 4 °C and used within 2 d for pull-down assays or eluted with buffer containing 2.5 mM d-Desthiobiotin.

*Arp4–N-actin–NactNB complex.* *S. cerevisiae* genes coding for Arp4, Arp8, actin, Taf14, Ies1, Ies2, Ies3, Ies4, Ies5, and Nhp10 were combined in a single pFBDM vector using the MultiBac system<sup>52</sup>. Integration of genes from the pFBDM vector into the baculoviral genome was performed in DH10MultiBac cells (GenevaBiotech), baculovirus generation in *Spodoptera frugiperda* Sf21 insect cells (IPLB-Sf21AE Invitrogen), and protein co-expression in *Trichoplusia ni* High Five insect cells (BTI-TN-5B1-4 Invitrogen) according to a published protocol<sup>52</sup>. High Five cells were transfected 1/100 (v/v) with baculovirus. Cells were cultured for 60 h at 27 °C until they were collected by centrifugation. Cells were lysed by sonication in 50 mM Tris pH 8, 300 mM NaCl, 5% glycerol, and 1× protease inhibitor cocktail (Sigma-Aldrich). The raw cell lysate was cleared by centrifugation. NactNB-bound Strep-Tactin Sepharose was used to isolate the Arp4–N-actin heterodimer from the soluble cell extract. The Arp4–N-actin–NactNB complex was washed with 50 mM Tris pH 8, 300 mM NaCl, and 5% glycerol and eluted with 50 mM Tris pH 8, 300 mM NaCl, 5% glycerol, and 2.5 mM d-Desthiobiotin. The ternary complex was further purified by ion-exchange chromatography with a HiTrapQ HP column (GE Healthcare; linear gradient 100 mM to 1 M NaCl) and gel filtration with a Superdex 200 column (GE Healthcare) equilibrated with 20 mM HEPES pH 8 and 200 mM NaCl. Pure protein was concentrated to a final concentration of 16–20 mg ml<sup>-1</sup>, flash frozen in liquid nitrogen, and stored at –80 °C.

**Arp8 module.** Genes encoding *S. cerevisiae* Arp4 and actin were cloned into one pFBDM vector and those coding for *S. cerevisiae* Arp8 (residues 255–881; the non-conserved N-terminal residues 1–254 were deleted<sup>27</sup>) and Ino80<sup>HSA</sup> (residues 462–598) carrying a C-terminal StrepTag II were combined on a second pFBDM vector<sup>52</sup>. Baculoviruses for the respective vectors were generated in Sf21 insect cells as described above. For the co-expression of the four proteins, High Five insect cells (BTI-TN-5B1-4 Invitrogen) were co-infected with the two viruses (1/100 (v/v) each), cultivated for 60 h at 27 °C, and collected by centrifugation. High Five cells were lysed by sonication in 20 mM HEPES pH 7.8, 100 mM KCl, 2.5% glycerol, and 1× protease inhibitor cocktail (Sigma-Aldrich). The complex was purified from the cleared cell lysate by affinity chromatography using Strep-Tactin Sepharose (IBA), ion exchange chromatography with a HiTrapQ HP column (GE Healthcare; linear gradient 100–800 mM NaCl), and gel filtration with a Superdex 200 column (GE Healthcare) equilibrated with 20 mM HEPES pH 8, 150 mM KCl, 2.5% glycerol, and 1 mM dithiothreitol. Peak fractions containing homogenous Arp8 module complex were pooled, concentrated, flash frozen, and stored at –80 °C.

For the Arp8 module Ino80–HSAα2 mutant (see Supplementary Table 1 for the mutated sequence range), a single pACE-BacI vector encoding expression cassettes for *S. cerevisiae* Arp4, actin, Arp8 (residues 255–881), and Ino80–HSAα2 (residues 462–598 + C-terminal StrepTag II) was generated by using the latest MultiBac system<sup>24,52</sup>. Generation of the baculovirus, expression in High Five insect cells, and purification of the wild-type and the HSAα2 mutant Arp8 module in complex with NactNB were performed in principle as described above. Prior purification of the respective complex 1 mg of purified NactNB (purification of NactNB is described above) was added directly to 20 ml of cleared insect cell lysate. Further purification followed the procedure described before for the wild-type Arp8 module.

**INO80 complex.** Purification of recombinant expressed *S. cerevisiae* INO80 complex from insect cells will be published elsewhere (unpublished data by: Krietenstein Nils, Oberbeckmann Elisa, Niebauer Vanessa, Schall Kevin, Schwarz Marianne, Moldt Manuela, Korber Philipp, Hopfner Karl-Peter, and Eustermann Sebastian). Briefly, two Baculoviruses were generated by MultiBac technology<sup>52</sup> using coding sequences for *S. cerevisiae* Ino80(2x Flag), Rvb1, Rvb2, Arp4,

Arp5-His, Arp8, Actin, Taf14, Ies1, Ies2, Ies3, Ies4, Ies5, Ies6, and Nhp10 subcloned into pFBDM vectors. For expression, High Five insect cells (BTI-TN-5B1-4 Invitrogen) were co-infected with the two baculoviruses 1/100 (v/v) each. INO80 complex was purified from the insect cells according to a previous published protocol<sup>16</sup> which resulted in a pure and monodisperse sample.

INO80 complex HSA mutants were prepared as described for wild-type INO80. Three Ino80(2x Flag) HSA mutants (HSAα1, HSAα2, or HSAα1/α2) were generated using standard cloning techniques and integrated into above-described Baculovirus using MultiBac technology<sup>52</sup> (mutated residues are shown in Supplementary Fig. 4e and Supplementary Table 1).

**Preparation of human mononucleosomes.** Canonical human histones were essentially purified as described previously<sup>53</sup>.

Briefly, *E. Coli* BL21 (DE3) cells (Novagen) were used to express histones for 2 h at 37 °C. Cells were disrupted using non-denaturing conditions and inclusion bodies were washed using 1% Triton X-100. Guanidinium chloride (7 M) was used for resuspension and inclusion bodies were dialyzed in urea (8 M). Cation exchange chromatography was applied to purify histones. After refolding of histones under low-salt conditions, an anion exchange chromatography step was used as a final purification step. Histones were lyophilized for long-time storage. To assemble histone octamers, single histones were resuspended in 7 M guanidinium chloride, mixed at a 1.2-fold excess of H2A/H2B, and dialyzed against 2 M NaCl for 16 h. Size exclusion chromatography (Superdex 200 16/600 column; GE Healthcare) was used to purify histone octamers, which were then stored in 50% glycerol at –20 °C. For the purpose of mononucleosome reconstitution we used fluorescein-labeled Widom 601 DNA<sup>54</sup> with 80 bp extranucleosomal DNA in the O/N0 orientation<sup>55</sup> or without extranucleosomal DNA (O/N0). After amplification by PCR, the DNA was purified using anion exchange chromatography and concentrated by applying vacuum. Histone octamers and DNA were mixed at 1.1-fold excess of DNA at 2 M NaCl. The sodium chloride concentration was then decreased to a final concentration of 50 mM over 17 h at 4 °C. In a final step, NCPs were purified using anion exchange chromatography. After dialysis to 50 mM NaCl, NCPs were concentrated to 1 mg ml<sup>-1</sup> and stored at 4 °C.

**Crystallization.** *Arp4–N-actin–NactNB.* Before crystallization the Arp4–N-actin–NactNB complex (16 mg ml<sup>-1</sup>) was mixed with subtilisin (1:6,000 (w/protease)/w(complex)) for in-drop proteolysis, 0.2 mM CaCl<sub>2</sub>, and either 1 mM ATP (buffered at pH 7.5 in 100 mM Tris) for the N-actin ATP-bound structure or with 1 mM ADP (buffered at pH 7.5 in 100 mM Tris) for the nucleotide-free (apo) structure. Crystals were grown by hanging-drop vapor diffusion at 20 °C in 1.4–1.5 M sodium malonate at pH 6.0. The best diffracting crystals were harvested after 4–8 d and cryo-protected with 23% glycerol.

*Ino80<sup>HSA</sup>–Arp4–N-Actin–Arp8.* For the crystallization of the Ino80<sup>HSA</sup>–Arp4–N-Actin–Arp8 complex, protein solution (13 mg ml<sup>-1</sup>) was mixed with LatA (for the LatA stock solution LatA was dissolved in 100% dimethylsulfoxide to a final concentration of 10 mM) at a molar ratio of 1:1.5 (complex/LatA). Crystals were grown by hanging-drop vapor diffusion at 4 °C against 0.1 M sodium citrate tribasic dihydrate and 18% w/v polyethylene glycol 3,350. The crystals were collected after 30 d and cryo-protected with 20% glycerol.

**Data collection and processing, structure determination, and refinement.** Diffraction data from all crystals were collected at 100 K with a wavelength of 1.0 Å at the Swiss Light Source beamline X06SA. Data were processed with *XDS*<sup>56</sup> and scaled with *POINTLESS* and *AIMLESS* within the CCP4 suite<sup>57</sup>.

**Arp4–N-actin–NactNB.** The two structures of the Arp4–N-actin–NactNB complex with N-actin ATP bound (Protein Data Bank (PDB) 5NBM) and nucleotide-free (apo) (PDB 5NBL) were determined by molecular replacement with Phaser<sup>58</sup>. For a first model, structures of *S. cerevisiae* actin (PDB 1YAG) and Arp4 (PDB 3QB0) were used as search models following the removal of any nucleotides, water molecules, or metal atoms. A homology model of NactNB was generated using the PHyre server<sup>59</sup> and the three complementarity-determining region loops were deleted before its use as a search model. Sequential search analyses with two copies of each of the search models for Arp4, actin, and NactNB resulted in a unique solution for two copies of the ternary complex per asymmetric unit. The initial model was used as search model for the analysis of the diffraction data sets from crystals grown in presence of ATP or ADP giving immediately a single solution with two complexes per asymmetric unit for both structures. In crystals grown with ATP, N-actin was clearly ATP bound. In contrast, in crystals grown in presence of ADP, N-actin was nucleotide-free. First models were then improved by iterative rounds of model refinement with *phenix.refine*<sup>60</sup> and manual model building with COOT<sup>34</sup>. Both electron density maps contain density for a peptide of unknown source that we could not assign to any sequence of the expressed proteins. This density was therefore modeled as a poly-UNK (unknown amino acid) peptide. The final model of the N-actin(ATP)–Arp4–NactNB complex (PDB 5NBM) at 3.4 Å resolution has R<sub>work</sub>/R<sub>free</sub> values of 15.2%/19.3% and the model of the N-actin(apo)–Arp4–NactNB complex (PDB 5NBL) at 2.8 Å resolution has R<sub>work</sub>/R<sub>free</sub> values of 17.1%/20.4% (Table 1).

*Ino80<sup>HSA</sup>–Arp4–N–Actin–Arp8*. The Ino80<sup>HSA</sup>–Arp4–N–Actin–Arp8 structure (PDB [5NBN](#)) was determined by molecular replacement with Phaser<sup>38</sup>. The Arp4–N–actin–NactNB structure (PDB [5NBM](#)) without NactNB and the yeast Arp8CTD structure (PDB 4AM6) were used as search models following the removal of any ligands or waters molecules. A single solution containing two copies of the Arp4–N–actin–Arp8 complex per asymmetric unit was found. Clear difference density for the Ino80<sup>HSA</sup> domain was visible in the initial map after molecular replacement. The model was improved through iterative rounds of refinement with *phenix.refine*<sup>60</sup>, applying secondary structure restraints and NCS restraints, and manual model building with COOT<sup>34</sup>. The Ino80<sup>HSA</sup> domain was built manually with COOT<sup>34</sup> using B-factor sharpening and feature-enhanced maps<sup>61</sup> (calculated by *phenix.fem*) for model building. Density for bound nucleotides at the canonical nucleotide binding sites of Arp4 and N–actin could be identified as ATP. Building and refinement of ADP into the unbiased density map showed in both cases clear difference density for a missing gamma-phosphate. Subsequent refinement shows similar B-factors for the alpha, beta, and gamma phosphate of each ATP molecule. The final model of the Ino80<sup>HSA</sup>–Arp4–N–Actin–Arp8 complex at 4.0 Å resolution has  $R_{\text{work}}/R_{\text{Free}}$  values of 19.3%/24.2% (Table 1).

Structures were analyzed using COOT<sup>34</sup> and PISA<sup>62</sup>. Superposition of structures was performed by using the Secondary Structure Matching<sup>33</sup> algorithm in COOT<sup>34</sup>. Figures of structures were prepared with PyMOL<sup>63</sup> and ChimeraX<sup>64</sup>.

**Affinity enrichment mass spectrometry.** Yeast with a double FLAG-tagged INO80 (Genotype: MATa INO80-FLAG<sub>2</sub> his3Δ200 leu2Δ0 met15Δ0 trp1Δ63 ura3Δ0; kindly provided by X. Shen)<sup>6</sup> were grown for 2 d in YPD medium at 30 °C. Cells were collected by centrifugation. Pellets were re-suspended 5:1 (w/yeast)/w(buffer)) in 20 mM HEPES pH 7.8. The cell suspension was dripped into liquid nitrogen and the frozen cells were lysed using a freezer mill (SPEX SamplePrep). The frozen cell powder was stored at –80 °C until usage.

Frozen yeast cell powder (20g) was thawed in 20 ml lysis buffer (25 mM HEPES pH 8.0, 500 mM KCl, 10% glycerol, 0.05% NP40, 1 mM EDTA, 4 mM MgCl<sub>2</sub>, and 1× protease inhibitor cocktail (Sigma-Aldrich)). Chromatin was fragmented with a polytron homogenizer (Kinematica; Fisher Scientific) and by sonication (Bransonic). The raw cell lysate was cleared by centrifugation and 250 µg ml<sup>−1</sup> avidin (IBA) was added.

The specific-binder nanobody (NactNB) and the control nanobody (enhancer GFP nanobody; eGFP-NB)<sup>65</sup> both had a C-terminal Twin-Strep-Tag and were expressed and purified as described for above for NactNB. NactNB or eGFP-NB immobilized on Strep-Tactin Sepharose were incubated with equal amounts of cleared yeast cell lysate. Unbound protein was removed by washing with buffer W1 (25 mM HEPES pH 8.0, 500 mM KCl, 10% glycerol, 0.05% NP40, 1 mM EDTA, and 4 mM MgCl<sub>2</sub>) followed by buffer W2 (25 mM HEPES pH 8.0, 200 mM KCl, 10% glycerol, 1 mM EDTA, and 4 mM MgCl<sub>2</sub>).

Samples for liquid chromatography-tandem mass spectrometry measurement were in principle prepared as published before<sup>66</sup>. Briefly, equal amounts of the nanobody Strep-Tactin Sepharose beads from each pull-down were incubated in buffer E1 (50 mM Tris-HCl pH 7.5, 2 M urea, 5 µg ml<sup>−1</sup> trypsin (Promega), and 1 mM dithiothreitol) for 30 min at 30 °C for on-bead digest. Any remaining peptides were eluted from the beads and alkylated with buffer E2 (50 mM Tris-HCl pH 7.5, 2 M urea, 5 mM iodoacetamide). Elution fractions were pooled and incubated in the dark overnight at 32 °C. The digestion was stopped by the addition of 1% trifluoroacetic acid. Samples were loaded on self-made C18 reversed-phase StageTips for purification and enrichment following a standard protocol<sup>67</sup>. Peptides were eluted with 2×20 µl buffer B (80% ACN and 0.5% AcOH) and concentrated using a SpeedVac concentrator to a final volume of 5–10 µl. Finally, 2.5 µl buffer A\* (2% ACN, 1% TFA) and 2.5 µl buffer A (0.5% AcOH) were added to the sample.

Peptide samples were measured on a liquid chromatography-tandem mass spectrometry system using an ultra-high performance liquid chromatography system (EASY-nLC 1000) coupled to an LTQ Orbitrap Elite (both Thermo Scientific) equipped with a standard nanoelectrospray source. Peptides were loaded onto a 15-cm × 0.050-mm inner diameter reversed phase column packed with 2 µm C18 beads (Acclaim PepMap RSLC analytical column, Thermo Scientific) and subsequently separated using a 90-min gradient of solvent B (98% ACN, 0.1% FA) from 2% to 35% at a flow rate of 250 nL min<sup>−1</sup>.

\*.RAW files from the eGFP-NB (mock) and NactNB triplicate experiments were analyzed together using the MaxQuant software suite (version 1.5.2.18) including the label-free algorithm for label-free quantification intensity calculation<sup>68</sup>. Downstream data analysis was performed in the Perseus environment (version 1.5.0.9)<sup>69</sup>. Briefly, label-free quantification intensity values were log<sub>10</sub> transformed, the data were filtered for at least two valid values in at least one of the two conditions, and missing values were imputed using a normal distribution at the noise level (width: 0.3 s.d. of the data; down shift: 1.8 s.d. of the valid data). To reveal significant outliers, a two-sample *t*-test was performed and data were visualized using an in-house R script.

**Fluorescence anisotropy.** Arp8 module in solution 40 bp dsDNA binding affinity was measured by fluorescence anisotropy in principle as described before<sup>70</sup>.

Equimolar amounts of the two complementary DNA strands (forward 5'-3': fluorescein-CCCTGGCGACTTCGCCTCGTTGGCGATTTCTTAGCAAA TATTCTTTC and reverse 5'-3': GAAAGAATTTGCTAACAGAAAATCGCCA

AAACGAGGCCGAAGTCGCCAGGG), solved in water, were heated to 95 °C for 10 min and slowly cooled at room temperature to anneal the two DNA strands. Arp8 module was diluted to the respective working concentration and incubated with 20 nM dsDNA on ice for 30 min in 20 mM Tris pH 7.8, 50 mM KCl, and 2.5% glycerol in a total volume of 100 µl. Fluorescence anisotropy was measured in a black flat-bottomed non-binding 96-well plate (Greiner-Bio) on a Tecan Infinite M1000 plate reader (excitation wavelength 470 nM, emission wavelength 520 nM).

Data were analyzed and fitted to a non-linear, non-cooperative 1:1 binding model ( $y = Af - (Af - Ab)x/(x/(Kd + x))$ ;  $y$  anisotropy;  $Af$  anisotropy of free ligand;  $Ab$  Anisotropy of bound ligand;  $Kd$  dissociation constant;  $x$  receptor concentration) with the program Prism (GraphPad) to calculate the dissociation constants for the respective complex. Experiments were performed in triplicate.

**EMSA.** The Arp8 module binding preference for mononucleosomes with or without extranucleosomal DNA was examined with competition EMSAs.

Increasing amounts of Arp8 module were titrated against a 1:1 mixture of 0N0 and 0N80 (20 nM each) mononucleosomes in 10 mM HEPES pH 8.0, 2 mM MgCl<sub>2</sub>, 60 mM NaCl, 8% glycerol, and incubated for 20 min on ice. Then, 15 µl of each titration step were loaded on a precast native polyacrylamide gel (NativePAGE Novex 4–16% Bis-Tris Protein Gels; Invitrogen). Arp8 module bound and unbound nucleosomes were resolved by Native-PAGE in 1× NativePAGE Running Buffer (Invitrogen; according to the manufacturer protocol) at 120 V for 120 min at 4 °C. Gels were analyzed on a Typhoon FLA 9000 plate reader (GE Healthcare) with 25 µm pixel size, using FITC fluorescence scan.

To test the binding capability of INO80 to nucleosomes, a titration of the complex was carried out. Increasing amounts of the protein in 25 mM Hepes, pH 8.0, 60 mM KCl, 7% glycerol, and 1 mM CaCl<sub>2</sub> were incubated with 20 nM 0N80 nucleosomes for 30 min on ice. INO80 bound and unbound nucleosomes were resolved by NativePAGE (Novex 4–16% Bis-Tris Protein Gels; Invitrogen) and subsequently visualized on a Typhoon FLA 9000 plate reader as described above.

**Nucleosome sliding assays.** The nucleosome sliding activity of INO80 was monitored on 0N80 mononucleosomes.

INO80 (18 nM) was incubated with 90 nM 0N80 nucleosomes in sliding buffer (25 mM Hepes, pH 8.0, 60 mM KCl, 7% glycerol, 0.10 mg ml<sup>−1</sup> BSA, 0.25 mM dithiothreitol, 2 mM MgCl<sub>2</sub>) at 26 °C. The sliding reaction was started by the addition of ATP and MgCl<sub>2</sub> (final concentrations: 1 mM ATP and 2 mM MgCl<sub>2</sub>). At the respective time points (30, 60, 120, 300, 600, 1,800, and 3,600 s), the reaction was stopped by adding lambda DNA (NEB) to a final concentration of 0.2 mg ml<sup>−1</sup>. NativePAGE (NativePAGE Novex 4–16% Bis-Tris Protein Gels; Invitrogen) was used to separate distinct nucleosome species. Gels were visualized on a Typhoon FLA 9000 plate reader as described above.

**ATPase assays.** In order to determine the ATPase rate of INO80, we applied an NADH-based ATPase assay in principle as described in<sup>24,71</sup>.

Briefly, 27 nM INO80 was incubated in assay buffer (25 mM Hepes, pH 8.0, 50 mM KCl, 5 mM MgCl<sub>2</sub>, 0.1 mg ml<sup>−1</sup> BSA) with 0.5 mM phosphoenolpyruvate, 2 mM ATP, 0.2 mM NADH, and 25 units ml<sup>−1</sup> lactate dehydrogenase/pyruvate kinase (unit is a measure for the amount of the enzymes and defined by the vendor Sigma-Aldrich) in a final volume of 50 µl at 30 °C. The Tecan Infinite M100 (Tecan) was used to monitor the NADH dependent fluorescence signal in non-binding, black, 384-well plates (Greiner) at an excitation wavelength of 340 nm and an emission wavelength of 460 nm over a time course of 40 min. ATPase activity for all samples was determined at conditions of maximum INO80 wild-type ATPase activity. Stimulation was performed with 50 nM 0N80 nucleosome, 100 nM 0N0 nucleosome, or 100 nM 223 bp DNA (DNA template used to reconstitute 0N80 nucleosomes). The final ATP turnover rate was calculated using maximal initial linear rates, which were corrected for a buffer blank.

The genome-wide *in vitro* reconstitution assay and the restriction enzyme accessibility assay are described in the Supplementary Note.

**Reporting Summary.** Further information on research design is available in the Nature Research Reporting Summary linked to this article.

**Data availability.** Coordinates and structure factors have been deposited in the PDB under accession codes [5NBM](#) for the N–actin(ATP)–Arp4–NactNB module, [5NBL](#) for the N–actin(apo)–Arp4–NactNB module, and [5NBN](#) for the Ino80<sup>HSA</sup>–Arp4–N–actin–Arp8 structures. Data for the genome-wide nucleosome positioning experiments reported in this paper have been deposited in the Gene Expression Omnibus under accession number [GSE113401](#). All other data and materials are available from the corresponding author on reasonable request.

## References

50. Rothbauer, U. et al. Targeting and tracing antigens in live cells with fluorescent nanobodies. *Nat. Methods* **3**, 887–889 (2006).
51. Conrath, K. E. et al. Beta-lactamase inhibitors derived from single-domain antibody fragments elicited in the camelidae. *Antimicrob. Agents Chemother.* **45**, 2807–2812 (2001).

52. Trowitzsch, S., Bieniossek, C., Nie, Y., Garzoni, F. & Berger, I. New baculovirus expression tools for recombinant protein complex production. *J. Struct. Biol.* **172**, 45–54 (2010).
53. Dyer, P. N. et al. Reconstitution of nucleosome core particles from recombinant histones and DNA. *Methods Enzymol.* **375**, 23–44 (2004).
54. Lowary, P. T. & Widom, J. New DNA sequence rules for high affinity binding to histone octamer and sequence-directed nucleosome positioning. *J. Mol. Biol.* **276**, 19–42 (1998).
55. Levendosky, R.F., Sabantsev, A., Deindl, S. & Bowman, G.D. The Chd1 chromatin remodeler shifts hexasomes unidirectionally. *eLife* **5** (2016).
56. Kabsch, W. XDS. *Acta Crystallogr. D Biol. Crystallogr.* **66**, 125–132 (2010).
57. Winn, M. D. et al. Overview of the CCP4 suite and current developments. *Acta Crystallogr. D Biol. Crystallogr.* **67**, 235–242 (2011).
58. McCoy, A. J. et al. Phaser crystallographic software. *J. Appl. Crystallogr.* **40**, 658–674 (2007).
59. Kelley, L. A., Mezulis, S., Yates, C. M., Wass, M. N. & Sternberg, M. J. The Phyre2 web portal for protein modeling, prediction and analysis. *Nat. Protoc.* **10**, 845–858 (2015).
60. Adams, P. D. et al. PHENIX: a comprehensive Python-based system for macromolecular structure solution. *Acta Crystallogr. D Biol. Crystallogr.* **66**, 213–221 (2010).
61. Afonine, P. V. et al. FEM: feature-enhanced map. *Acta Crystallogr. D Biol. Crystallogr.* **71**, 646–666 (2015).
62. Krissinel, E. & Henrick, K. Inference of macromolecular assemblies from crystalline state. *J. Mol. Biol.* **372**, 774–797 (2007).
63. *The PyMOL Molecular Graphics System, Version 1.8.* (Schrodinger, LLC, 2015).
64. Goddard, T. D. et al. UCSF ChimeraX: meeting modern challenges in visualization and analysis. *Protein Sci.* **27**, 14–25 (2018).
65. Kirchhofer, A. et al. Modulation of protein properties in living cells using nanobodies. *Nat. Struct. Mol. Biol.* **17**, 133–138 (2010).
66. Keilhauer, E. C., Hein, M. Y. & Mann, M. Accurate protein complex retrieval by affinity enrichment mass spectrometry (AE-MS) rather than affinity purification mass spectrometry (AP-MS). *Mol. Cell. Proteomics* **14**, 120–135 (2015).
67. Rappaport, J., Mann, M. & Ishihama, Y. Protocol for micro-purification, enrichment, pre-fractionation and storage of peptides for proteomics using StageTips. *Nat. Protoc.* **2**, 1896–1906 (2007).
68. Cox, J. et al. Accurate proteome-wide label-free quantification by delayed normalization and maximal peptide ratio extraction, termed MaxLFQ. *Mol. Cell. Proteomics* **13**, 2513–2526 (2014).
69. Tyanova, S. et al. The Perseus computational platform for comprehensive analysis of (proteo)omics data. *Nat. Methods* **13**, 731–740 (2016).
70. Favicchio, R., Dragan, A. I., Kneale, G. G. & Read, C. M. Fluorescence spectroscopy and anisotropy in the analysis of DNA-protein interactions. *Methods Mol. Biol.* **543**, 589–611 (2009).
71. Kianitsa, K., Solinger, J. A. & Heyer, W.-D. NADH-coupled microplate photometric assay for kinetic studies of ATP-hydrolyzing enzymes with low and high specific activities. *Anal. Biochem.* **321**, 266–271 (2003).

## Reporting Summary

Nature Research wishes to improve the reproducibility of the work that we publish. This form provides structure for consistency and transparency in reporting. For further information on Nature Research policies, see [Authors & Referees](#) and the [Editorial Policy Checklist](#).

### Statistical parameters

When statistical analyses are reported, confirm that the following items are present in the relevant location (e.g. figure legend, table legend, main text, or Methods section).

n/a Confirmed

- The exact sample size ( $n$ ) for each experimental group/condition, given as a discrete number and unit of measurement
- An indication of whether measurements were taken from distinct samples or whether the same sample was measured repeatedly
- The statistical test(s) used AND whether they are one- or two-sided  
*Only common tests should be described solely by name; describe more complex techniques in the Methods section.*
- A description of all covariates tested
- A description of any assumptions or corrections, such as tests of normality and adjustment for multiple comparisons
- A full description of the statistics including central tendency (e.g. means) or other basic estimates (e.g. regression coefficient) AND variation (e.g. standard deviation) or associated estimates of uncertainty (e.g. confidence intervals)
- For null hypothesis testing, the test statistic (e.g.  $F$ ,  $t$ ,  $r$ ) with confidence intervals, effect sizes, degrees of freedom and  $P$  value noted  
*Give P values as exact values whenever suitable.*
- For Bayesian analysis, information on the choice of priors and Markov chain Monte Carlo settings
- For hierarchical and complex designs, identification of the appropriate level for tests and full reporting of outcomes
- Estimates of effect sizes (e.g. Cohen's  $d$ , Pearson's  $r$ ), indicating how they were calculated
- Clearly defined error bars  
*State explicitly what error bars represent (e.g. SD, SE, CI)*

*Our web collection on [statistics for biologists](#) may be useful.*

### Software and code

Policy information about [availability of computer code](#)

Data collection

Data collection software at the Swiss Light Source (Villigen, Switzerland) MX beamlines (DA+ GUI).

Data analysis

XDS (version May 1, 2016 BUILT=20160617)  
 CCP4 Suite (version 7.0.017) including Pointless version 1.10.26; Aimless version 0.5.27; Phaser (version 2.6.1)  
 PHENIX (version 1.11.1\_2575)  
 COOT (version 0.8.8)  
 MaxQuant software suite (version 1.5.2.18)  
 Perseus (1.5.0.9)  
 Bowtie  
 DANPOS

For manuscripts utilizing custom algorithms or software that are central to the research but not yet described in published literature, software must be made available to editors/reviewers upon request. We strongly encourage code deposition in a community repository (e.g. GitHub). See the Nature Research [guidelines for submitting code & software](#) for further information.

## Data

Policy information about [availability of data](#)

All manuscripts must include a [data availability statement](#). This statement should provide the following information, where applicable:

- Accession codes, unique identifiers, or web links for publicly available datasets
- A list of figures that have associated raw data
- A description of any restrictions on data availability

Coordinates and structure factors have been deposited in the Protein Data Bank under PDB ID accession codes 5NBM for the N-actin(ATP)-Arp4-NactNB, 5NBL for the N-actin(apo)-Arp4-NactNB and 5NBN for the Ino80HSA-Arp4-N-Actin-Arp8-module structures.

Data of the genome-wide nucleosome positioning experiments reported in this paper have been deposited on the NCBI Gene Expression Omnibus (accession number GSE113401).

All other data and material are available from the corresponding author upon reasonable request.

## Field-specific reporting

Please select the best fit for your research. If you are not sure, read the appropriate sections before making your selection.

Life sciences       Behavioural & social sciences       Ecological, evolutionary & environmental sciences

For a reference copy of the document with all sections, see [nature.com/authors/policies/ReportingSummary-flat.pdf](http://nature.com/authors/policies/ReportingSummary-flat.pdf)

## Life sciences study design

All studies must disclose on these points even when the disclosure is negative.

Sample size	not applicable for x-ray structure determination (PDB validation report is attached). Affinity enrichment mass spectrometry (AE MS) using the nanobody (Figure 2b) was performed in triplicates and statistically evaluated as previously described by Keilhauer et al. Mol Cell Proteomics 14, 120-35 (2015). All biochemical experiments with Arp8-module or INO80 were performed in triplicates. INO80 genome-wide in vitro reconstitution assay were performed in duplicates.
Data exclusions	no data were excluded
Replication	all attempts of replication were sucessful
Randomization	no randomization
Blinding	no blinding

## Reporting for specific materials, systems and methods

### Materials & experimental systems

n/a	Involved in the study
<input checked="" type="checkbox"/>	<input type="checkbox"/> Unique biological materials
<input type="checkbox"/>	<input checked="" type="checkbox"/> Antibodies
<input type="checkbox"/>	<input checked="" type="checkbox"/> Eukaryotic cell lines
<input checked="" type="checkbox"/>	<input type="checkbox"/> Palaeontology
<input checked="" type="checkbox"/>	<input type="checkbox"/> Animals and other organisms
<input checked="" type="checkbox"/>	<input type="checkbox"/> Human research participants

### Methods

n/a	Involved in the study
<input checked="" type="checkbox"/>	<input type="checkbox"/> ChIP-seq
<input checked="" type="checkbox"/>	<input type="checkbox"/> Flow cytometry
<input checked="" type="checkbox"/>	<input type="checkbox"/> MRI-based neuroimaging

## Antibodies

### Antibodies used

Arp4-N-actin binding nanobody (identified in this study).

### Validation

The specificity of the nanobody has been evaluated by AE MS experiments (Figure 2B) and by using x-ray crystallography.

## Eukaryotic cell lines

Policy information about [cell lines](#)

Cell line source(s)

Yeast with a double FLAG-tagged INO80 (Genotype: MAT $\alpha$  INO80-FLAG2 his3Δ200 leu2Δ0 met15Δ0 trp1Δ63 ura3Δ0) were kindly provided by X. Shen (The University of Texas MD Anderson Cancer Center, Smithville, Texas, USA) and has been previously described in Shen et al. Nature 406, 541-4 (2000).  
Spodoptera frugiperda Sf21 insect cells (Invitrogen; 11497013)  
Trichoplusia ni High Five insect cells (Invitrogen; B85502)

Authentication

INO80 purifications described in Shen et al. Nature 406, 541-4 (2000) were successfully repeated.  
Insect cells lines from Invitrogen were not further authenticated.

Mycoplasma contamination

Protein expression cell lines were not tested.

Commonly misidentified lines  
(See [ICLAC](#) register)

not applicable